論文 / 著書情報
Article / Book Information

題目(和文)	
Title(English)	Study on Near-infrared Photodetectors with a Liquid Crystalline Phthalocyanine Derivative for Biomedical Applications
著者(和文)	カビール シャリアル
Author(English)	Shahriar Kabir
出典(和文)	学位:博士(工学), 学位授与機関:東京工業大学, 報告番号:甲第12380号, 授与年月日:2023年3月26日, 学位の種別:課程博士, 審査員:飯野 裕明,梶川 浩太郎,間中 孝彰,宮島 晋介,田口 大,藤井 彰彦
Citation(English)	Degree:Doctor (Engineering), Conferring organization: Tokyo Institute of Technology, Report number:甲第12380号, Conferred date:2023/3/26, Degree Type:Course doctor, Examiner:,,,,,
学位種別(和文)	博士論文
Type(English)	Doctoral Thesis

Study on Near-infrared Photodetectors with a Liquid Crystalline Phthalocyanine Derivative for Biomedical Applications

A dissertation submitted to the
Department of Electrical and Electronic Engineering, School of Engineering
Tokyo Institute of Technology

In partial fulfillment of the requirements for the degree of
Doctor of Engineering

Submitted by

Shahriar Kabir

Supervised by

Hiroaki Iino

February 2023

Abstract

The first near-infrared (NIR-I) window is defined as the wavelength range from 700 nm to 1000 nm and can be used to monitor the vital signals of a human being for consumer and biomedical applications. In order to fabricate organic photodetectors that can be used in such specific applications, it is necessary to investigate active materials with good absorption in this spectral window. 1,4,8,11,15,18,22,25-octaoctyl-phthalocyanine ($8H_2Pc$) is a liquid crystalline (LC) organic semiconductor material which not only meets this condition but also shows good solubility in common organic solvents and high ambipolar carrier mobility in columnar LC phases exhibited between 86°C and 149°C. In this work, the phthalocyanine derivative, $8H_2Pc$, and a fullerene derivative, phenyl-C61-butyric-acid-methyl ester ($PC_{61}BM$) were used as a donor-acceptor (DA) pair to fabricate NIR organic photodetectors (OPDs) for biomedical applications. The OPDs were fabricated with varying DA blend ratios, different device architectures, and on top of rigid and flexible substrates. The champion device was prepared in the inverted architecture with 1:1 w/w ratio of blend materials and it exhibited external quantum efficiency of 60%, responsivity of 0.4 A/W, and shot-noise-limited specific detectivity of 3×10^{12} Jones at 760 nm with -1 V reverse bias. The condition of the bulk heterojunction active layer was observed with polarized optical microscopy, atomic force microscopy, and X-ray diffraction measurements and the effect of annealing at different temperatures, annealing time, and cooling rate on the bulk heterojunction and OPD performance was investigated and discussed. Finally, the practical usability of the champion OPD in this study was demonstrated by monitoring the photoplethysmogram signal of a human subject with a simple experimental setup.

Contents

Chapter 1
Introduction

1.1 Background and Motivation

In recent years organic electronics have attracted notable research attention due to advantages such as large-area and large-scale manufacturing [1, 2], solution processability [3, 4], mechanical flexibility, stretchability, and skin conformity [5, 6, 7], low-temperature and low-cost fabrication, among others. In the field of light emitting diodes, solar cells, and photodetectors, organic electronics have advanced significantly in the past few years [8, 9, 10, 11]. The possibility of changing the semiconducting and material properties of polymers and small molecules by making modifications to their chemical structure has driven the research and development in these fields. Since C. W. Tang reported the first ever single heterojunction organic solar cell with power conversion efficiency of 0.95% and fill factor of 0.65 in 1986 [12], many more innovative approaches have been investigated to improve the performance of organic photovoltaic devices. Example of such an innovative technology is the hybrid organic-inorganic perovskite solar cells [13]. This emerging technology is promising because of the rapid progress it has shown in recent years by being initiated in 2009 with an efficiency of 3.8% and reaching a lab-scale power conversion efficiency of 23.3% in 2018 [14]. However, perovskite solar cells make use of the material lead (Pb) which is toxic to living organisms and faces challenge to ensure durable outdoor operation [14]. Such challenges emphasize the necessity of exploring novel technologies and materials to realize more efficient and sustainable devices. On that note, in the area of organic photodetectors (OPD), very high specific detectivity of 10^{13} Jones has been achieved in recent years which is comparable to the state-of-the-art inorganic photodetectors [15]. In 1995, the concept of bulk heterojunction with a mixture of donor and acceptor (DA) materials was introduced in the fabrication of polymer photovoltaic cells [16] and photodiodes [17] and has been shown to be more efficient than the single heterojunction system in terms of photon absorption and dissociation of exciton. This concept has opened up new avenues of research into OPDs as it was revealed that the performance of the devices depends significantly on the blend ratio of materials, grain size and purity, crystalline condition, surface morphology, thickness of the active layer, to name a few. Furthermore, it allowed the discovery of novel types of photodetector operation such as photomultiplicative, charge collection narrowing, and charge injection narrowing types of OPDs [18, 19, 20].

Without any photocurrent gain mechanism, the external quantum efficiency of an OPD cannot go beyond 100% due to carrier recombination and other losses [21, 22]. Very interestingly, this limit can be exceeded by the photomultiplication effect which can be enabled by adjusting the weight ratio of donor and acceptor materials from 1:1 (non-gain mode OPDs) to 100:1 (photomultiplication mode OPDs) as reported with the P3HT:PC$_{61}$BM and P3HT:PC$_{71}$BM bulk heterojunction systems [18, 23, 24]. On the other hand, the concept of charge collection narrowing was introduced very recently in 2015 by Armin et. al. where narrowband spectral detection was achieved at the absorption onset of the blend materials by using a thick bulk heterojunction [19]. Narrowband light detection is of research and industrial interest because of the applications of different wavelengths of light in different fields. From extremely high energy radiation such as gamma rays to low energy radiation such as radio waves, each have their unique applications and are indispensable part of our everyday life. For the detection and application of such electromagnetic radiation, photodetectors are essential electronic devices that have stayed relevant for over a century of research, commercial, and industrial applications. Moreover, to address the demands of innovative approaches in the modern technological age, flexible, wearable, and skin conformal photodetectors are being investigated and realized [5, 25, 26]. In addition to novel structures of devices and modes of operation, it is worthwhile to explore various materials and material combinations for clarifying their relative advantages and disadvantages. Liquid crystalline (LC) semiconductors are one such unique type of materials that show one or more intermediary phases between crystalline and liquid phases. By making use of the intermediary phase, or mesophase, it is possible to change the orientation of molecules, influence the crystalline order, grain size and purity of the thin film even after fabrication [27, 28, 29]. LC materials with large π-conjugated systems have the ability to self-organize into single domain thin films by taking advantage of the presence of the LC mesophase. As a result, boundaries between randomly oriented grains in the crystalline phase, which create large barriers for charge and exciton transport, can be avoided [30, 31]. Moreover, solution processed LC thin films have been reported to be a good precursor for films having excellent morphology and uniformity [29, 32]. Investigating such materials in the field of bulk heterojunction photodetectors for efficient detection of near-infrared light is appealing as an exciting and meaningful research theme.

As the world population is nearing 8 billion in 2023 with an increasing ratio of elderly populace, healthcare and wellbeing service industry has seen a tremendous rise in attention [33]. Especially, during the height of the COVID-19 pandemic, medical diagnosis techniques and equipment have been developed and improved and continue to be improved today as the effects of the pandemic have not concluded yet [34, 35]. On an additional personal note, my grandmother passed away in 2001 after she accidentally slipped in the washroom and didn’t recover even after receiving medical care near our village home. As I started my graduate studies in electrical and electronic engineering, my personal motivation from the beginning was to connect my research with medical care for the elderly citizens and other patients. I imagined a comfortable and non-invasive system of health monitoring with flexible devices that could be worn by elderly people during their daily life activities and thus any anomaly in their health could be detected and proper care could be provided as soon as possible. During my research work, I have worked towards that goal to the best of my abilities and in this thesis, I have reported near-infrared photodetectors based on a liquid crystalline organic semiconductor in bulk heterojunction active layer on rigid and flexible substrates and discussed the principal factors influencing their optical and electrical characteristics in bulk heterojunction active layer. I have addressed the issue of air stability and reliability of the organic devices and presented the strategies to mitigate the degradation of device performance. Finally, I have highlighted the practical utility of the organic photodetectors by using the champion device to detect and monitor the vital signal of a human subject in real time.

1.2 Photodetector Operation Principle

In simple terms, a photodetector is a device that converts an incident ray of photons (or light energy) into electric current (or electrical energy). By definition, photodetector covers the devices of photodiodes and phototransistors. While a photodiode is a vertical device, meaning that the carriers move in the vertical direction towards the electrodes, a phototransistor is a horizontal device. As in this study, photodiodes were investigated and so for the sake of simplicity, photodetector will refer to photodiode in this thesis.

In a photodetector, the current is actually the result of an electron-hole exciton pair generation and separation inside the active material of the heterojunction photodetector, which consisted of DA molecules. In detailed terms, the generation of photocurrent can be explained in four consecutive steps in terms of their efficiencies: photon absorption with efficiency η_A, exciton diffusion where η_{ED} is the fraction of excitons reaching the DA interface, generated charge transfer exciton and the exciton dissociation at the DA interface with efficiency η_{CT}, and finally, the collection of carriers at the electrodes with efficiency η_{CC} [36]. These four steps and their efficiencies vary in different materials and material combinations, grain size and purity, morphological condition of the active layer, and operation conditions. Thus, vast numbers of research have been conducted and are still being conducted to find the optimum condition for best performance of different types of photodetectors and elucidate the factors behind them.

As a photodetector converts light energy into electrical energy, it is capable of operating with or without external power sources. If a photodetector is operated without an external power source i.e., without external bias, it operates in the photovoltaic mode. In this mode, the photodetector operates as the same as a solar cell. On the other hand, when a photodetector is operated with external bias, it operates in the photoconductive mode. The schematic illustrations of these two operational modes are shown in Fig. 1.1.

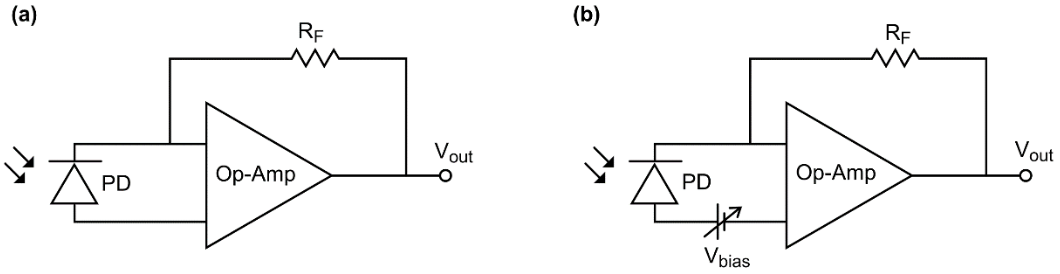

Figure 1.1. Photodiodes operating in (a) photovoltaic and (b) photoconductive mode

Next, as a photodetector is an opto-electronic device, it is important to consider the strategies to reduce the optical loss as much as possible and efficiently illuminate the active layer for maximum photon absorption. A photodiode has two electrodes, anode and cathode, and one of these is usually fabricated using a transparent or semi-transparent conductive material in order to facilitate the transmission of light. Popular choices for this purpose are tin-doped indium oxide (ITO), silver (Ag), zinc oxide (ZnO), and Poly(3,4-ethylenedioxythiophene)-poly(styrenesulfonate) (PEDOT:PSS). Innovative and novel materials such carbon nanotubes and nanowires have also emerged as viable options in recent years.

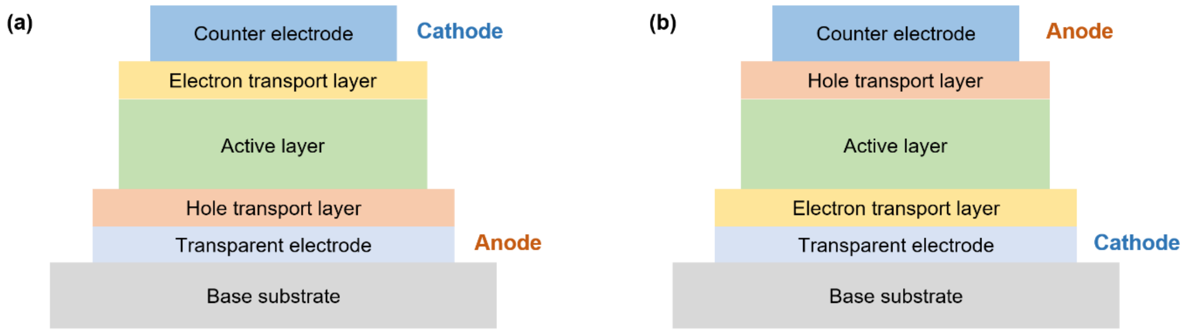

Figure 1.2. Schematic illustrations of (a) conventional and (b) inverted architecture of OPDs.

Depending on the role of this transparent electrode, photodiodes can be divided into two categories: conventional and inverted photodiodes. In the case of a conventional photodiode, the transparent electrode generally operates as the anode and the other electrode, typically made with aluminum (Al), operates as the cathode [4]. In an inverted photodiode, the operation of the electrodes is just the opposite, hence the use of the term “inverted”. Different surface modifiers are used to tune the work function of the transparent electrode for this purpose [37, 38]. As shown in Fig. 1.2 (b), the counter electrode in inverted photodetectors is usually stable metals such as gold (Au) or silver (Ag).

Depending on the range of the spectral detection window, photodetectors can be divided into two categories as well: broadband and narrowband. Broadband photodetectors, also referred to as panchromatic photodetectors, have a relatively flat spectral detectivity over a wide range of electromagnetic radiation spectrum. On the other hand, narrowband photodetectors are selective to a certain range of the electromagnetic spectrum. Both types of photodetectors are useful in practical situations depending on the specific application.

1.3 Figures of Merit for Photodetectors

To objectively compare different photodetectors, there are several well-established figures of merit. The most commonly used figures of merit for photodetectors are responsivity, external quantum efficiency, specific detectivity, noise equivalent power, linear dynamic range, and cutoff frequency among others. The definition and brief description of these quantities are presented below.

1.3.1 Responsivity

Responsivity (R) is defined as the ratio of photocurrent to the intensity of the incident light. It is a measure of how much photocurrent is generated in the photodetector with respect to the strength or intensity of the incident light.

Responsivity of a photodetector can be calculated using the following equation:

$$R = \frac{J_{photo}}{I_{light}};\ J_{photo} = J_{illuminated} - J_{dark} \tag{1}$$

Here $J_{illuminated}$, J_{dark}, and I_{light} stands for the output current density during illuminated condition, output current density during dark condition, and intensity of incident light, respectively. The unit of R is A/W.

1.3.2 External Quantum Efficiency

External quantum efficiency (EQE) is defined as the number of charge carriers collected by the device electrodes to the number of photons of a given energy shining from the outside of the device. It can be considered as a measure of how many incident photons can be converted into charge carriers by the particular device. EQE can be calculated using the following equation:

$$EQE = \frac{R}{\mathrm{q}} \times \frac{hc}{\lambda} \tag{2}$$

Here R, q, h, c, and λ stand for responsivity, unit charge, Plank's constant, speed of light, and wavelength of incident light, respectively.

There is one more photodetector parameter called the internal quantum efficiency (IQE) which can be calculated from EQE by removing the loss components due to reflectance and parasitic absorptions [39]. IQE is a measure of how efficiently the active material can convert absorbed photons into charge carriers without taking the losses associated with the photon absorption process into account.

1.3.3 Noise Equivalent Power

Noise equivalent power (NEP) is defined as the signal power that gives a signal-to-noise ratio of 1 in a 1 Hz bandwidth. NEP is a measure of the lowest intensity of incident light that the detector can distinguish from background noise levels. The unit of NEP is W/Hz$^{1/2}$.

1.3.4 Specific Detectivity

Specific detectivity (D^*) is defined as the reciprocal of the device noise equivalent power normalized per square root of the device area times the frequency bandwidth. It is a measure of how sensitive the PD is with respect to the incident light of a particular wavelength. It can be calculated using the following equation:

$$D^* = \frac{\sqrt{A\Delta f}}{NEP} \tag{3}$$

Here *A, Δf,* and *NEP* stand for the device area, frequency bandwidth, and noise equivalent power of the device, respectively.

If it assumed that the shot noise is the dominant contributor to the dark current of the device, then the shot-noise-limited-detectivity (D^*_{sh}) can be calculated using the following equation:

$$D^*_{sh} = \frac{R}{\sqrt{2qJ_{dark}}} \tag{4}$$

Here R, q, and J_{dark} stand for responsivity, unit charge, and dark current density, respectively. The unit of D* is $\mathrm{cmHz^{1/2}W^{-1}}$ (Jones).

1.3.5 Linear Dynamic Range

Linear dynamic range (LDR) is defined as the maximum range of light intensities for which the output current is linearly proportional to the intensity of incident light. LDR is a measure of the range of light intensities under which the device can perform accurately with a linear output.

LDR of a PD can be calculated using the following equation:

$$LDR = 20\log\left(\frac{J_{lin,max}}{J_{lin,min}}\right) \tag{5}$$

1.3.6 Cutoff Frequency

Cutoff frequency (f_c) is defined as the frequency at which the amplitude of the output signal falls to $1/\sqrt{2}$ (approximately 70%) of the signal at low frequency or at DC. It is a measure of how fast the device response is under varying light input. It can be measured directly or estimated using the following equation:

$$f_c = \frac{0.35}{t_r} \tag{6}$$

Here t_r stands for rise time of the device output signal. The frequency bandwidth can also be calculated from the cutoff frequency.

1.3.7 Carrier Mobility

For evaluating the charge carrier mobility in different bulk heterojunction conditions, the technique of extracting injected charge carriers using the charge extraction by linearly increasing voltage (CELIV) method was utilized as proposed by G. Juška et al. [40]. As this method uses a metal-insulator-semiconductor (MIS) device structure, it will be referred to as the MIS-CELIV method in this thesis. The mobility of holes and electrons can be extracted using the following two equations:

$$\mu = \frac{2d_s^2}{At_{tr}^2} \times (1 + \frac{\varepsilon_s d_i}{\varepsilon_i d_s}) \tag{7}$$

$$t_{tr} = \frac{4}{\pi} t_{2j0} \tag{8}$$

Here, ε_s and ε_i represent the relative dielectric permittivity, and d_s and d_i represent the thickness of the active layer and insulator layer, respectively. A represents the rate of change of the extraction voltage, and t_{tr} represents the carrier transport time. As shown in eq. (8), t_{tr} can be calculated from the characteristic time, t_{2j0}, which is the time required to reach twice the value of j_0, which in turn can be found from the transient current waveshapes of charge extraction.

1.4 Near-infrared Light and its Applications

Near-infrared (NIR) radiation is a subset of electromagnetic radiation with wavelength longer than the visible window. As such, humans are unable to detect NIR light without any external visual aid. Although being invisible to human visual perception, NIR sensing photodetectors have applications in a variety of technologies such machine vision [41], night vision [42], medical monitoring [25], food safety and quality inspection [43, 44], and bioimaging [45]. One such spectral region of interest is the first near-infrared (NIR-I) window which corresponds to the region of electromagnetic radiation with wavelength spanning from about 700 to 1000 nm [46]. The NIR-I window is uniquely useful for the purpose of biomedical applications such as pulse oximetry, photoplethysmography, vein detection, etc.

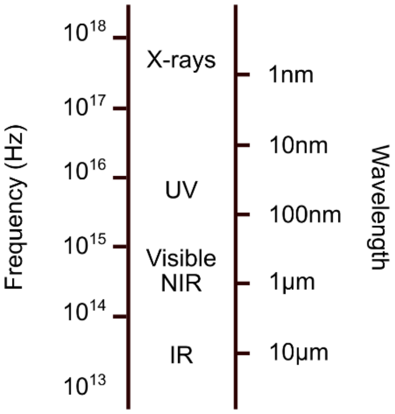

Figure 1.3. Simplified representation of the electromagnetic spectrum.

Traditionally, NIR sensing has been realized with photodetectors fabricated with single-crystal inorganic semiconductor materials such as Si, Ge, GaInAs for their advantageous properties such as high charge-carrier mobility, small exciton binding energy, and high air stability and reliability. However, they typically have drawbacks including costly processing [47], mechanical inflexibility [11], and operation in cryogenic temperatures [48, 49]. Apart from single-crystal inorganic semiconductors, hydrogenated amorphous silicon (a-Si:H) has shown promise as an inorganic option to prepare mechanically flexible devices, but there are also challenges such as high defect density, high dark current, and low carrier mobility in a-Si:H films. Taking all of these into account, organic semiconductors are favorable for the fabrication of NIR photodetectors because of their high absorption in the NIR region [50, 51, 52], solution processability over large area [53], non-toxicity, simple and low-cost fabrication methods, and good mechanical flexibility [54, 55]. Nevertheless, in order to be practically viable, organic photodetectors have to reach the industry standard photosensitivity levels of Si PIN photodiodes, reported to be 0.52 A/W at 830 nm [56]. Therefore, it is necessary to explore organic semiconductor materials to emulate the performance standards of inorganic semiconductor devices without sacrificing the exciting properties of flexibility and low-cost.

1.5 Organic Semiconductors

Organic semiconductors are semiconducting materials that are constituted of pi-bonded molecules or polymers made up of mainly carbon and hydrogen. There are several major differences in the charge carrier generation and transport mechanism of organic and inorganic semiconductors. Typical inorganic semiconductor such as Ge, Si, and GaAs have low energy bandgaps of 0.67 eV, 1.1 eV, and 1.4 eV, respectively. Therefore, in these materials free charge carriers can be generated by thermal excitation even at room temperature. The typical range of conductivity of these materials is about 10^{-8} to 10^{-2} $\Omega^{-1}cm^{-1}$. On the other hand, conductivity of organic semiconductors is extrinsic, and it results from charge carrier injection from external electrodes, doping of materials and dissociation of photogenerated electron-hole pairs [57]. The absorption and emission of light take place typically in the range of 2 ~ 3 eV in organic semiconducting materials. Commonly known organic semiconductors are pentacene, Cn-benzothieno-benzothiophene (Cn-BTBT), poly(3-hexylthiophene-2,5-diyl) (P3HT) among others and they have found extensive utility in the applications of organic light emitting diode (OLED), organic field effect transistor (OFET), organic solar cell (OSC), and OPD [58, 59, 60]. Historically, organic semiconductors have been used in xerographic copiers and laser printers as well. Compared to inorganic semiconductors, organic semiconductors have their own set of advantageous properties. Such as, organic materials are suitable for fabrication of solution processed devices at low temperatures with large active areas. Large-scale manufacturing is also possible by utilizing the techniques of inkjet printing or roll-to-roll fabrication. Organic semiconductor devices can be fabricated even on flexible substrates with a variety of geometrical degrees of freedom [61]. In addition, by tuning the chemical structure of the molecular organic materials, the spectral sensitivities of the devices can be tailored for the respective application. OLEDs are being used extensively in high-definition display technologies while OFETs, OSCs, and OPDs are being investigated and developed for industrial usage. Lastly, organic semiconductors can be based on small molecules such as pentacene, or it can be long repeating chain of molecules, also called a polymer, such as P3HT. Semiconducting polymers are attractive because of their low cost, ease of processibility and good mechanical properties [62]. However, the polymerization reaction is inherently difficult to synthesize and reproduce polymer semiconductor with the exact molecular weight. Small molecule semiconductors can circumvent this issue as they can be synthesized and reproduced reliably and precisely.

1.6 Liquid Crystalline Semiconductors

Liquid crystalline materials exhibit a state of matter that is in between crystalline solids and isotropic liquids. There are many different types of liquid crystal phases, which are most commonly distinguished on the basis of their optical properties, such as optical textures. The unique textures result from the different molecular arrangements and orientations within the grains of the material. Within a single pure grain, the molecules are usually well-ordered. But the direction of orientation between different grains can be different and so the textures are distinct from one phase of LC material to another.

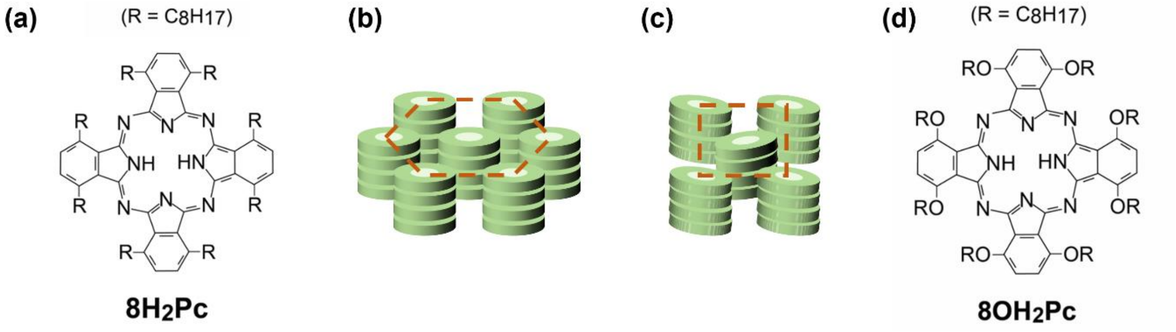

Figure 1.4. (a) Chemical structure of liquid crystalline $8H_2Pc$ material, schematic illustration of the molecular arrangement in (b) Col_h and (c) Col_r phases, (d) Chemical structure of crystalline $8H_2Pc$ material.

Figure 1.4 (a) shows the chemical structure of 1,4,8,11,15,18,22,25-octaoctyl-phthalocyanine ($8H_2Pc$) which is an organic semiconductor material with LC properties. The molecules of this material are shaped like a disc, and it exhibits two discotic LC phases: columnar rectangular (Col_r, 86 °C to 98 °C) phase and columnar hexagonal (Col_h, 98 °C to 149 °C) phase [63]. The availability of these mesophases can be seen in the differential scanning calorimetry (DSC) thermogram as shown in Fig. 1.5 (a). In the Col_h and Col_r phases, the columns of the molecules are aligned in hexagonal and rectangular patterns, respectively. When columns are aligned on perpendicular on the substrate, the LC films in the Col_h and Col_r phases show no retardation and some retardation, respectively, while observing through polarized microscope, because the molecules in the Col_r phase are titled in each column. A generalized schematic diagram of the orientation of the molecules in these two LC phases is shown in the Fig. 1.4 (b) and (c). $8H_2Pc$ demonstrates high carrier mobility with maximum hole mobility of 0.2 cm^2/Vs in the LC phase measured by the time-of-flight technique [64]. $8H_2Pc$ is also highly soluble in common organic solvents at room temperature and so it is possible to prepare thin film devices by solution process at low cost. Finally, this LC material has high absorbance in the NIR spectrum region which makes it a suitable candidate for fabricating narrowband NIR photodetectors.

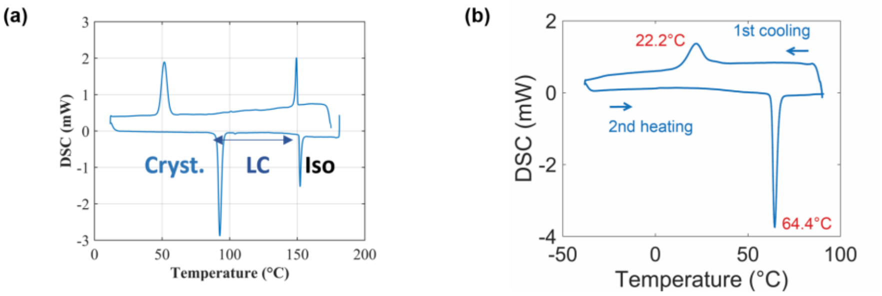

Figure 1.5. DSC thermograms of (a) $8H_2Pc$ and (b) $8OH_2Pc$.

In addition to the LC $8H_2Pc$ material, another organic semiconductor, 1,4,8,11,15,18,22,25-octaoctyloxy-phthalocyanine ($8OH_2Pc$), was utilized in this study to compare the optical and electronic performance. Contrary to $8H_2Pc$, the $8OH_2Pc$ material does not show any mesophase as it shows only one phase transition temperature from crystalline to liquid phase at 64ºC in the DSC thermogram (Fig. 1.5 (b)). Also as shown in Fig. 1.4 (d), the chemical structure of this material is very similar to $8H_2Pc$, and so they exhibit good absorption in the NIR window and good solubility in organic solvents making them very suitable for the fabrication of NIR photodetectors.

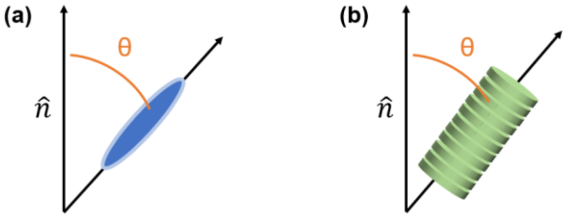

Fig. 1.6. Schematic illustration of the tilt angle θ between the (a) local director and the long axis for a rod-like molecule and (b) local director and the columnar axis for a disc-like molecule. Here, it was assumed that the individual disc-like molecules do not have any tilt angle with respect to the columnar axis.

An established method of comparing the degree of the orientation of the molecules is called the order parameter (S). S represents the orientational order of the molecules of the LC material with regards to the individual orientational deviation of the molecules from the director ($\hat{n}$). The director is the common axis along which the LC molecules show a tendency to be roughly pointed. It can be thought as the molecular direction of preferred orientation in LC mesophases. Typical value of S ranges from 0.3 to 0.9 which depends on the temperature of the sample. If the sample is in perfect order, the value of S is unity. The order parameter can be calculated with the following equation [65]:

$$S = \frac{1}{2} < 3cos^2\theta - 1 > \tag{9}$$

Here, θ denotes the angle between the local director and the long axis or columnar axis of each molecule or column. The <> brackets denote taking the average over all of the molecules or columns in the sample. In an isotropic liquid, the average of the cosine terms is zero, and therefore the order parameter evaluates to zero. On the other hand, in a perfect crystal, the order parameter evaluates to one. This same concept can be applied to rod-like and disc-like molecules as shown in Fig. 1.6. However, for disc-like molecules, the relative tilt angles of the individual molecules with respect to the columnar axis should also be considered for evaluating S which requires a much more extensive investigation of the sample [66]. Such a detailed analysis of the order parameter of disc-like materials is out of the scope of this study, so a relatively simple parameter of “degree of face-on orientation” was evaluated for the $8H_2Pc$ samples. For this purpose, the degree of face-on orientation was defined as the percentage of the sample area that achieved the face-on molecular orientation and it was evaluated from the peak intensity of the in-plane XRD spectra of the samples.

1.7 Objectives of This Study

Each photodetector is designed to serve one or more specific purposes and in order to do it efficiently, a photodetector must be sensitive in a certain spectral region where its responsivity is well defined. Thus, the primary objective of this study was to realize highly efficient NIR photodetectors with liquid crystalline semiconductor material and improving the performance by investigating the underlying factors that influence the optical and electrical characteristics. To objectively evaluate the sensitivity and efficiency of the photodetectors in a wide range of wavelengths and operation modes, the figures of merit such as responsivity, external quantum efficiency, and shot-noise-limited specific detectivity were chosen for their wide acceptance and reported values. In terms of these figures of merit, the objective was to achieve the state-of-the-art responsivity level of 0.5 A/W, external quantum efficiency of 50%, and shot-noise-limited specific detectivity of 10^{13} Jones within the NIR-I window, i.e., between 700 nm to 1000 nm wavelength. In addition, to affirm that the realized devices can be utilized in practical situations, the demonstration of vital signal monitoring of a human subject was aimed as one of the most important objectives of this study.

1.8 Organization of This Thesis

This thesis is organized in 6 chapters. In Chapter 1, the motivation and objectives for this study along with a brief introduction to photodetectors are given. In Chapter 2, the material preparation and device processing of the rigid and flexible photodetectors are presented. At the end of Chapter 2, the methods of characterizing and evaluating the photodetectors are described. The analysis of the optical and electrical characteristics of photodetectors prepared with the alkoxy phthalocyanine derivative, $8OH_2Pc$, are discussed in Chapter 3. These characteristics are analyzed based on the thin film condition such as intermixing condition, grain size and purity, and crystalline order of the active layer. Next, in Chapter 4, the optical and electrical characteristics and thin film condition of photodetectors based on the LC alkyl phthalocyanine derivative, $8H_2Pc$, are discussed and compared with the previous results. From this comparison, the unique features of LC materials in the performance of NIR photodetectors are presented. In Chapter 5, at first, the response speed, air stability, and reliability of the champion OPD are reviewed for practical application. After confirming the sufficient photo response, the practical utility of the champion device is demonstrated by monitoring the vital signal of a human subject in real time. As the OPD was also implemented on flexible plastic substrate, its mechanical flexibility and performance are also discussed in this chapter. Finally, the overall summary of this study and the future outlook are detailed in the last chapter.

Chapter 2

Experimental Methods

2.1 Material Preparation

To prepare the bulk heterojunction thin films of different DA blends, $8H_2Pc$ and $PC_{61}BM$ were mixed in weight ratios of 4:1, 1:1, and 1:4, and 20 mg/mL solutions in chloroform were prepared. In a similar fashion, $8OH_2Pc$ and $PC_{61}BM$ were mixed in weight ratios of 8:1, 4:1, 2:1, 1:1, 1:4, and 1:8, and each mixture was dissolved in chloroform for preparing solution with concentration of 20 mg/mL.

Poly(3,4-ethylenedioxythiophene)-poly(styrenesulfonate) (PEDOT:PSS, Clevios PVP Al 4083, purchased from Heraeus) solution was prepared by diluting the purchased solution to 0.125 wt% with isopropyl alcohol (IPA). To remove the large particles, the solution was filtered through a 45 µm PTFE filter.

For the fabrication of inverted photodetectors, poly(ethylenimine) ethoxylated (PEIE) solution was prepared by diluting the purchased solution to 0.4 wt% with ethanol.

To anneal the neat $8H_2Pc$ and $8H_2Pc$:$PC_{61}BM$ bulk heterojunction films, it was necessary to cover the samples with a sacrificial polymer layer. This polymer layer prevented dewetting during the thermal annealing at liquid crystalline temperature and enabled the reorientation of the molecules. To prepare the polymer solution, 2600 mg poly(methacrylic acid) (PMAA) was dissolved in 20 mL water to prepare a 13 wt% solution. As an additive, 650 mg (1/4 by weight of PMAA) ethylene glycol was added to the solution. The solution was stirred with a magnetic stirrer at 50°C, 800 rpm for 24 hours to obtain a homogeneous solution.

2.2 Preparation of Samples and Devices

2.2.1 Thin Films on SiO_2 and Glass Substrates

For evaluating the surface morphology, absorption spectrum, and optical texture of the bulk heterojunction active layer, thin films of the DA blend were prepared by spin-coating technique. The size of the SiO_2 and glass substrates was 25 mm × 20 mm. At first, SiO_2 substrates and glass substrates were cleaned by using detergent in ultra-pure water, IPA, and acetone in ultra-sonic baths. The substrates were dried, and then the active layer solution was spin-coated at 1000 rpm for 60 s at room temperature. A slope of 1 s was used to smoothly accelerate and decelerate the substrates during the spin-coating process. The thickness of the spin-coated films was approximately 250 nm as measured with a stylus profiler.

2.2.2 Annealed Samples on SiO_2 and Glass Substrates

After preparing the thin films on SiO_2 or glass substrates, the samples were covered with a PMAA polymer layer by spin coating the PMAA solution at 4000 rpm for 120 s. An acceleration slope of 5 s was used to smoothly distribute the solution over the surface of the thin film. Even after spin-coating the polymer layer contained a significant amount of residual water, so they were transferred inside a vacuum chamber and dried for 10 mins. After 10 mins, the samples were taken out and placed on a hot plate for thermal annealing.

As the liquid crystalline $8H_2Pc$ material shows two mesophases: columnar rectangular phase from 86°C to 98°C and columnar hexagonal phase from 98°C to 149°C, the samples were thermally annealed at 90°C and 140°C each for 30 mins and 1 min to observe the effect of annealing duration at different columnar phases.

In addition, to observe the effect of rate of cooling, a portion of the samples were slowly cooled down to room temperature at a rate of 3°C/min and another portion was rapidly cooled down to room temperature by placing the hot samples on a large metal sheet. Hereafter, these samples will be referred to as “TA90-Slow” (or “TA140-Slow”) and “TA90-Rapid” (or “TA140-Rapid”), respectively.

2.2.3 Photodetectors on Glass Substrates

As mentioned in Chapter 1.2, there are two architectures of photodiodes: conventional and inverted architecture. The fabrication process of the two devices is briefly discussed below:

i. Glass substrates patterned with indium tin oxide (ITO) were cleaned by using detergent in ultra-pure water, IPA, and acetone in ultra-sonic baths.

ii. To increase the surface wettability, the cleaned substrates were then treated with UV-ozone for 15 min.

iii. In case of conventional photodiodes, the next step was to spin-coat the PEDOT:PSS solution at 2000 rpm for 30 s at room temperature. During spin-coating, 1 s slope was used to smoothly accelerate and decelerate the substrates. The samples were then dried at 130°C for 10 min. For inverted photodiodes, 0.4 wt% PEIE solution was spin-coated at 3000 rpm for 30 s at room temperature. In this case, the slope was 4 s. The samples were then dried at 100 °C for 10 min.

iv. After drying, the active layer solution was spin-coated on the samples at 1000 rpm for 60 s at room temperature. Again, 1 s slope was used to smoothly accelerate and decelerate the substrates. The thickness of the active layer was approximately 250 nm as measured with a stylus profiler.

v. Next, for conventional photodiodes, 60 nm Al electrode was deposited on top of the active layer at 30 Å/s inside a vacuum chamber. For inverted OPDs, at first 3 nm layer of MoO_3 was deposited on top of the active layer at a rate of 0.2 Å/s. Finally, 60 nm Au electrode was deposited at a rate of 4 Å/s inside a vacuum chamber. The active area of the diodes was defined by using different shadow masks with openings of 1 mm^2 and 16 mm^2.

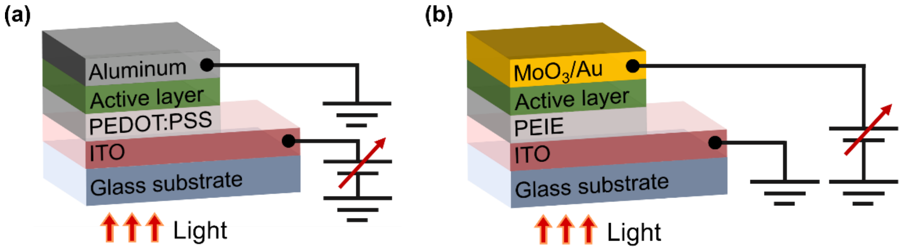

Figure 2.1. Schematic illustration of (a) conventional and (b) inverted photodiodes on rigid glass substrate.

2.2.4 Photodetectors on Flexible Substrates

i. Polyethylene terephthalate (PET) substrates (ルミラー T60) of 25 µm thickness were at first cut into approximately 18 mm × 18 mm pieces and then cleaned using detergent in ultra-pure water, IPA, and acetone in ultra-sonic baths. At the same time, glass substrates of approximately 22 mm × 22 mm size were also cleaned in the same method.

ii. Next, CYTOP (CTL-809A) was spin-coated on the glass substrates at 500 rpm for 30 s. After spin-coating, the PET substrates were pasted on top the CYTOP covered glass substrates.

iii. To firmly fix the PET substrate on the glass substrate, the samples were then baked at 80°C for 60 mins followed by a secondary bake at 130°C for 60 mins.

iv. Next, 60 nm Al electrode was thermally deposited on the substrates inside a vacuum chamber. A metal shadow mask was used to create the desired pattern of the electrode.

v. The samples were taken out of the vacuum chamber and a thin layer of PEIE was spin-coated at 3000 rpm for 60 s with a slope of 1 s at room temperature. The samples were then dried at 100°C for 10 min and then allowed to cool down to room temperature.

vi. After cooling down, the active layer was spin-coated on the samples at 1000 rpm for 60 s. Again, during this spin-coating process, 1 s slope was used to smoothly accelerate and decelerate the substrates.

vii. The substrates were then placed inside a vacuum chamber for depositing the counter electrode. This time, 20 nm Ag electrode was deposited on top of the active layer through a metal shadow mask. The thickness of the Ag electrode was chosen to be 20 nm because of its semi-transparency (27% at NIR wavelength of 740 nm) and relatively good electrical conductivity. The metal shadow mask defined the active area of the devices to be 1 mm^2 and 4 devices were prepared on each substrate.

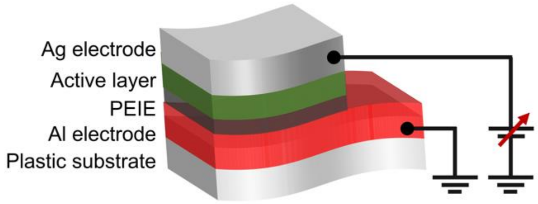

Figure 2.2. Schematic illustration of the flexible device on PET substrate

2.2.5 Encapsulation of Devices

To isolate the device from atmospheric effects, the device was encapsulated by using 2 glass substrates and epoxy glue (コニシボンド クイック5 エポキシ樹脂系接着剤). At first, the A type and B type glues were mixed in 1:1 ratio and deposited around the active area of the device using a thin needle. Next, a glass substrate was placed on top and allowed to rest for 10 min. When the epoxy glue hardened, it created a barrier layer and isolated the device from outside atmosphere as shown in Fig. 2.3.

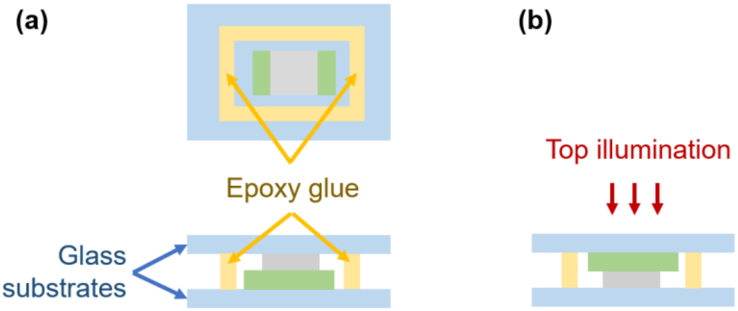

Fig. 2.3. (a) Top and side view of the encapsulated device with two glass substrates and epoxy glue. (b) Position of the device when illuminated from the top.

In addition to isolating the device from atmospheric effects, the encapsulation technique allowed the device to be illuminated either from the bottom or the top of the device as shown in Fig. 2.3 (b).

2.3 Sample and Device Characterization

2.3.1 Observation of Surface Morphology

The surface morphology of the thin film was observed, and the root mean square (RMS) roughness of the film surface was evaluated using the atomic force microscopy (AFM) in tapping mode. For this measurement, Seiko Instruments SPI3700 was used.

2.3.2 Observation of Optical Texture

While observing the thin films of different materials, the light is scattered by the molecules inside the film and results in different optical textures. By using a polarizer, polarizing optical microscopy (POM) can be used to evaluate the existence of different phases of the material or the orientation of the molecules in certain directions. For this observation, Nikon ECLIPSE LV100 microscope was used.

2.3.3 Observation of Optical Properties

As a general note, transmission, absorption, emission, reflection, refraction, diffraction, or scattering effects are the optical properties of a material when it interacts with light [67]. For semiconductors, these optical properties depend on the characteristics of the electronic bands or more specifically, the atomic structure, presence or absence of certain atoms, chemical bonding, etc [68]. As this study is on the topic of photodetectors, the absorption and transmission spectra of different materials and blend of materials were observed in the ultraviolet (UV), visible, and NIR windows. For this measurement, Hitachi Spectrophotometer U-3900H was used.

2.3.4 Evaluation of Dielectric Constant

To evaluate the dielectric constant (ε_r) of the $8H_2Pc$ material at different phases and investigate its temperature dependence, an LC cell with ITO electrodes and spacing of 3.68 µm and active area of 16 mm^2 was prepared and $8H_2Pc$ was injected into the cell at 160ºC. The LC cell was placed on top of a hot stage (Mettler Toledo) and the capacitance of the sample was measured with a precision LCR meter (Agilent 4284A) at different temperatures over a frequency range of 20 Hz to 1 MHz. The respective ε_r values were extracted using the following equation:

$$\varepsilon_r = \frac{Cd}{A\varepsilon_0} \tag{10}$$

Here, C, d, A, and ε_0 represent the capacitance of the sample, spacing between the electrodes, active area, and dielectric constant of air, respectively.

2.3.5 Electrical Characterization

The electrical characteristics of the photodetectors were evaluated in ambient air using a 740 nm surface mounted LED (OSA Opto Light GmbH, OCX-440 Star). The output light intensity of the LED was controlled by modulating the input voltage and the light intensity was measured with a silicon photodiode (ADCMT 82314A Optical Sensor). The current-voltage measurement data was collected using a source measurement unit (ADCMT 8252 Digital Electrometer). As the output light intensity of the LED could be quite strong (greater than 1 mW/cm^2), there was a possibility that significant number of excitons could be generated outside the active area of the device and enter the active area, resulting in overestimation of photodetector parameters. To prevent such an effect, and to evaluate the extent of the possible overestimation, the current-voltage characteristics were evaluated with and without a shadow mask with an opening of 16 mm^2. The schematic illustration of the experimental setup for this purpose is shown below [69].

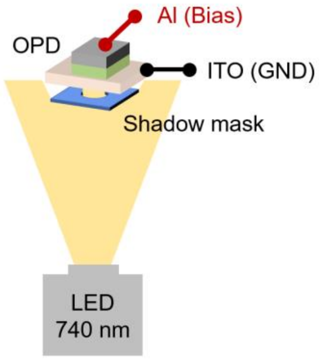

Fig. 2.4. Schematic illustration of the setup for measuring R, EQE, and D^*_{sh} in this study [69].

The measurement setup shown in Fig. 2.4 was also utilized for the evaluation of NEP of the photodetectors. In that case a chopper and neutral density filters were inserted in between the 740 nm LED and the shadow mask. The chopper was operated at ~10 Hz to measure the transient photoresponse of the OPD and NEP was calculated from the observations. The neutral density filters were used to modulate the intensity of the light.

In addition to evaluating the OPDs at the NIR wavelength of 740 nm, they were also evaluated over the wavelength range of 500 nm to 900 nm. For this purpose, a xenon lamp in combination with a monochromator controller (Koken Kogyo MD-1000), a mirror, and a convex lens was used as shown in the following figure [70].

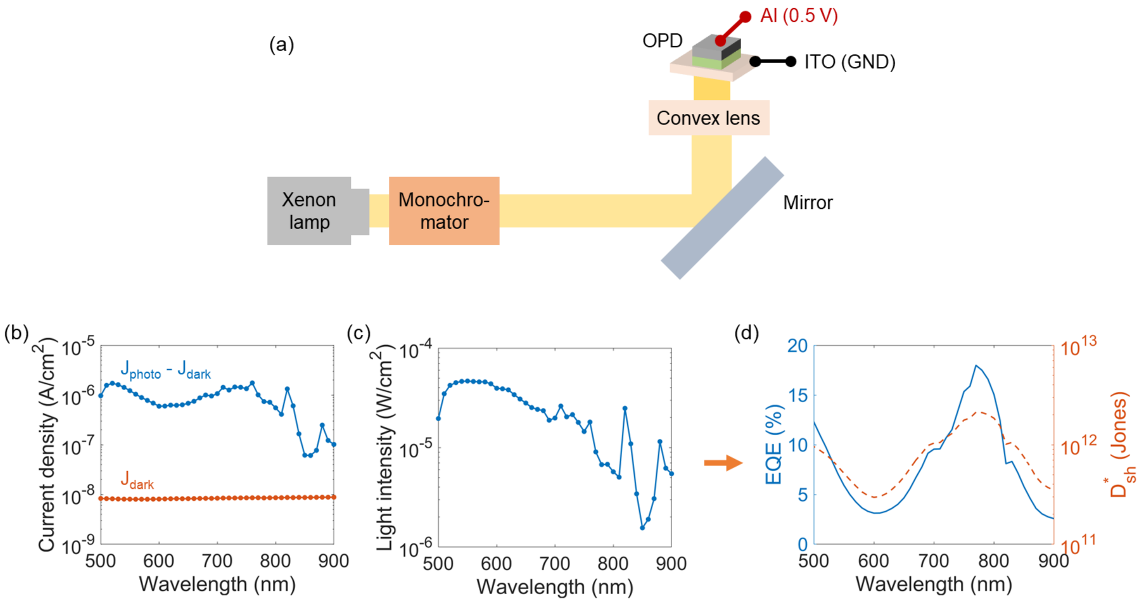

Fig. 2.5. (a) Schematic illustration of the measurement setup for R, EQE, and D^*_{sh}, (b) a representative measurement of J_{dark} and (J_{photo} - J_{dark}) spectra with a reverse bias voltage of -

0.5V, (c) light intensity spectra incident on the ITO electrode, and (d) calculated EQE and D^*_{sh} of the device [70].

To evaluate the cutoff frequency and transient photoresponse of the OPDs, a 740 nm LED with light intensity of 8 mW/cm^2 was used as the light source. The variable frequency input waveform was supplied using a multifunction synthesizer (NF Electronic Instruments Wavefactory 1941) and amplified by a high-speed power amplifier (NF Electronic Instruments 4010). The input and output waveforms were captured by an oscilloscope (LeCroy 312A 100MHz) with a load resistance of 10 kΩ.

2.3.6 DSC Measurement of Blend Material

$8H_2Pc$ and $PC_{61}BM$ were mixed in the ratio of 1:1 w/w and dissolved in a small amount of chloroform. The solution was then dried at 95°C without boiling the solvent. Next, the sample was placed inside a vacuum chamber for 30 min to completely remove the solvent. 3.4 mg of the dry sample was used to measure the DSC of the $8H_2Pc$:$PC_{61}BM$ blend sample. The differential scanning calorimeter DSC-60 manufactured by Shimadzu was used for this measurement.

2.4 Summary of Chapter 2

In this chapter, the methods of material preparation, the fabrication of thin film samples and photodetectors with conventional and inverted architecture on top of glass and plastic substrates were discussed in detail. The process of annealing the thin films in different conditions and device encapsulation was also reported. The method of evaluating the dielectric constant of $8H_2Pc$ and temperature dependence of this constant was also described. Finally, the measurement setup for the evaluation of the devices was explained with schematic illustrations and the procedure for DSC measurement of the $8H_2Pc$:$PC_{61}BM$ blend sample was described.

Chapter 3

8OH$_2$Pc:PC$_{61}$BM Near-infrared Organic Photodetectors

In this chapter, the optical and electrical characteristics of the organic photodetectors prepared with the blend of 8OH$_2$Pc and PC$_{61}$BM is reported. As shown in the following figure, the 8OH$_2$Pc material has very strong absorption in the NIR region with a peak at 770 nm [70]. This peak coincides with the peak of the liquid crystalline 8H$_2$Pc material, but much higher in intensity. Therefore, the 8OH$_2$Pc material was chosen initially for the fabrication of NIR photodetectors. In latter chapters, the performance of the photodetectors based on 8H$_2$Pc are compared with that of the ones based on 8OH$_2$Pc and the underlying differences are discussed in detail.

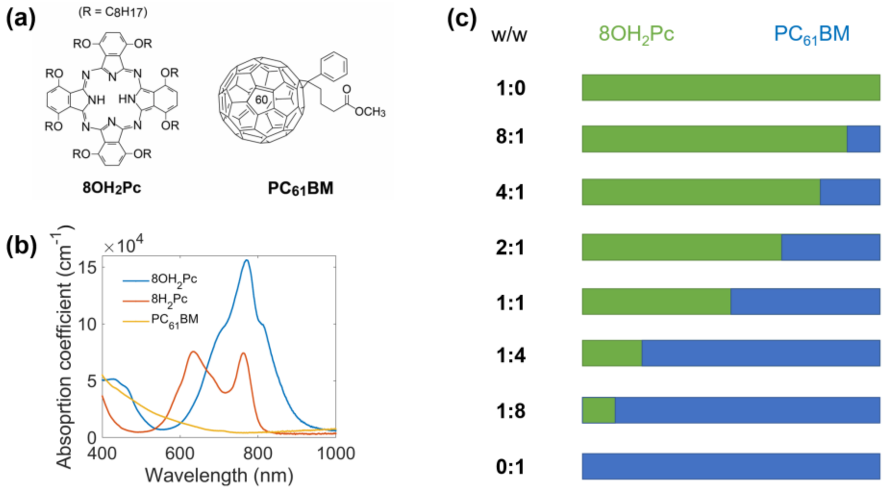

Fig. 3.1. (a) Chemical structures, (b) absorption spectra of the organic materials, and (c) visual representation of the blend ratios used for the fabrication of photodetectors in this study.

3.1 Optical Characteristics

Figure 3.2 shows the values of the absorption peak wavelengths and their equivalent photon energies for the thin films of neat 8OH$_2$Pc, neat PC$_{61}$BM, and different blend ratios [70]. Neat film of 8OH$_2$Pc showed a peak at 770 nm and two shoulders at 708 nm and 813 nm in the NIR window. These three peaks corresponded to 1.61 eV, 1.75 eV, and 1.53 eV, respectively. While the thin film of neat PC$_{61}$BM did not show any absorbance in this region, thin films of 8:1 to

1:8 blend samples all showed absorption peaks with gradually decreasing absorption coefficient and slight bathochromic shift as the ratio of $PC_{61}BM$ increased. From the position of the peaks, it was evident that the optical absorption of the $8OH_2Pc$:$PC_{61}BM$ system in the NIR window is contributed by the $8OH_2Pc$ material. It was interesting to note that in 4:1 and 2:1 blend samples, new absorption peaks were observed at 878 and 886 nm, respectively. These new absorption peaks might have resulted from the intermolecular interaction of $8OH_2Pc$ and $PC_{61}BM$, or the molecular aggregation of $8OH_2Pc$ in these samples changed to J-aggregate. The peak intensity at these new positions was higher in the 4:1 blend sample compared to the 2:1 one. Although the absorption peak at 781 nm became weaker in these two samples, it did not disappear completely, indicating that the new optical absorption mechanism coexisted with the previous one.

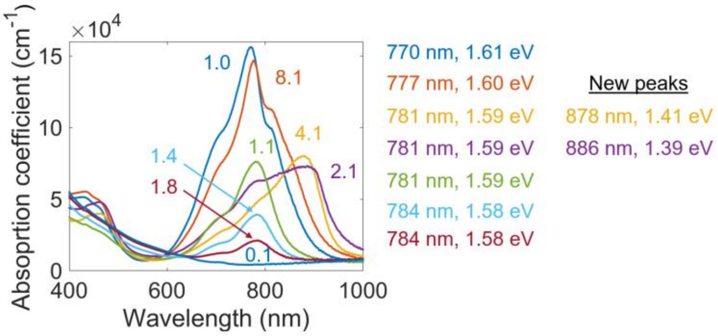

Fig. 3.2. Absorption spectra measurements of different blend samples with the peak position and photon energy corresponding to the peaks [70].

To clarify the principal reason of the new peaks, the dimeric interaction of $1OH_2Pc$ and $PC_{61}BM$ molecules was simulated computationally using density functional theory with the RWB97XD method at different sub-nanometer distances as shown in Fig. 3.3 [70]. Here, $1OH_2Pc$ stands for methoxy phthalocyanine and it was used for simulation to reduce the computational load while preserving the necessary parameters of electronic energy interactions of the original $8OH_2Pc$:$PC_{61}BM$ system. The purpose of this simulation was to confirm if the creation of charge transfer (CT) states in the bulk heterojunction could affect the absorption mechanism of the material system. The simulated absorption spectra in Fig. 3.4 indeed showed an extension to the longer NIR wavelengths for the $1OH_2Pc$:$PC_{61}BM$ dimer when the distance between the molecules were sufficiently close, 0.8 nm to be precise. Although this result showed a mathematical possibility of creation of interfacial CT states in the investigated bulk heterojunction system, it is unlikely for the $8OH_2Pc$ and $PC_{61}BM$ molecules to achieve such nanoscopic molecular distance in both 4:1 and 2:1 blend samples. Thus, it was concluded that the dimeric interaction of the $8OH_2Pc$ and $PC_{61}BM$ molecules were not the reason for the new absorption mechanism.

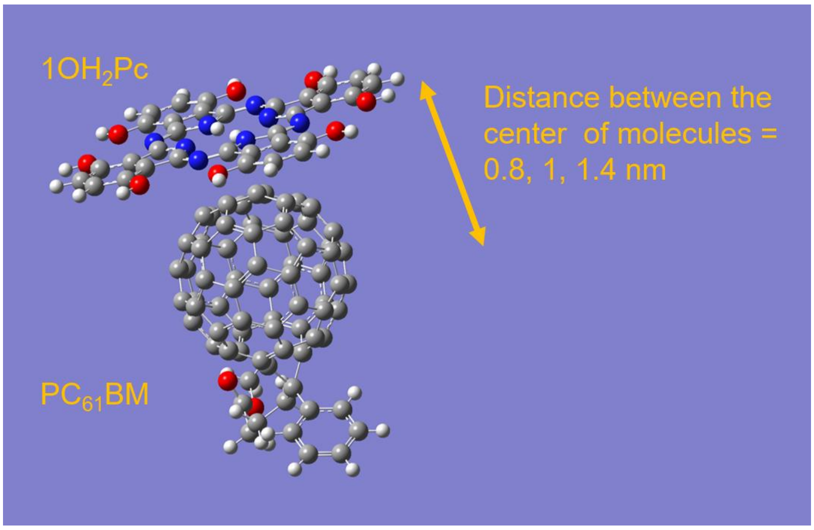

Fig. 3.3. 3D model of the $1OH_2Pc$ and $PC_{61}BM$ molecules showing the dimer system considered in this DFT simulation [70].

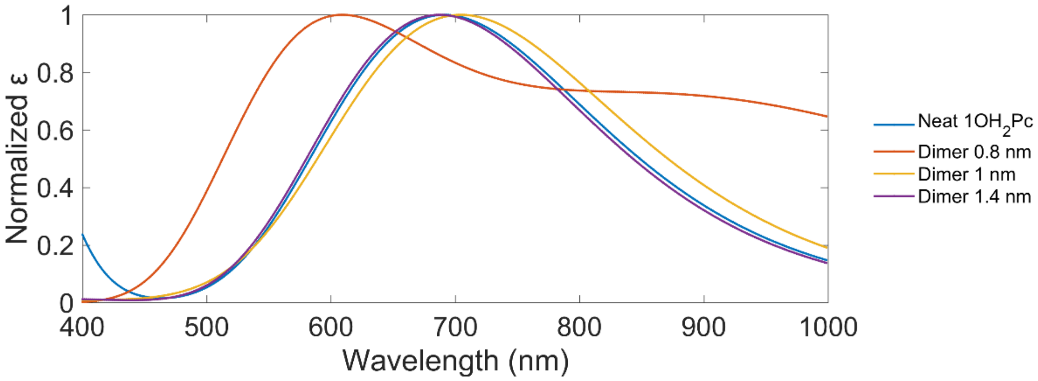

Fig. 3.4. Simulated absorption spectra of neat $1OH_2Pc$ material and $1OH_2Pc$:$PC_{61}BM$ dimer at different molecular distances [70].

Next, the possibility of change in molecular aggregation of $8OH_2Pc$ to J-aggregate was investigated by XRD measurement as shown in Fig. 3.5. It was observed that the peaks originated from the crystalline $8OH_2Pc$ material, not from the amorphous $PC_{61}BM$ material which showed no distinguishable peak in the XRD measurement. The small angle XRD patterns of the 1:0, 4:1, and 2:1 blend samples in Fig. 3.5 (c) showed that the peaks of 4:1 and 2:1 blend samples shifted slightly to smaller angle and the intensity of the peaks were higher, even compared to that of neat $8OH_2Pc$. The d-spacings of peaks of the 1:0, 4:1, and 2:1 blend samples were 19.4 Å, 18 Å, and 17.4 Å, respectively. It suggested that the crystalline structure and order of the $8OH_2Pc$ materials slightly changed (transitioned to J-aggregate) and the grain of the material increased in size, respectively. In these specific samples, most of the $8OH_2Pc$ molecules were considered to be ordered in the slipped-stack packing arrangement due to the π-π stacking of discotic molecules, accounting for the appearance of the new absorption peak at longer wavelengths [71]. Note that the XRD peak at 4.6° shown by neat $8OH_2Pc$ did not disappear completely in the 4:1 and 2:1 blend samples, indicating that not all $8OH_2Pc$ molecules transitioned to the J-aggregate crystal structure. That is why the original NIR absorption peak did not disappear completely, but the new absorption peak appeared beside it.

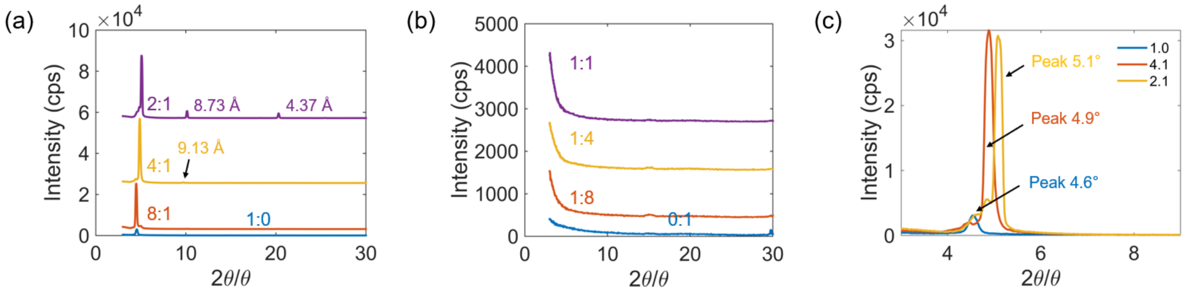

Fig. 3.5. (a, b) XRD spectra of thin films of neat $8OH_2Pc$, neat $PC_{61}BM$, and different blend ratios. (c) Small angle XRD spectra of the thin films of neat $8OH_2Pc$ and 4:1 and 2:1 blend samples.

Thus, the appearance of new absorption peaks was attributed to the J-aggregate type molecular packing of the $8OH_2Pc$ material in the bulk heterojunction thin films at specific blend ratio of 4:1 and 2:1 with $8OH_2Pc$:$PC_{61}BM$.

3.2 Electrical Characteristics

Figure 3.6 shows the dark and photo current-voltage characteristics of the devices prepared with 8:1 to 1:8 blend samples irradiated with 60 mW/cm^2 of 810 nm NIR light. All the devices showed idea diode performance and photo current output, but their performance depended significantly on the blend ratio of the materials. It was observed that the J_{photo} increased exponentially from the 8:1 to 1:4 blend samples and then decreased slightly at the final 1.8 sample. On the other hand, the J_{dark} on reversed bias increased less sharply from the 8:1 to 1:1 blend samples and then settled to a roughly steady value at 10^{-8} A/cm^2. As a result, the J_{photo}/J_{dark} ratio at revise bias of -0.5 V increased exponentially from the 8:1 to 1:4 blend samples, starting from 67 and reaching a peak at 2.3 × 10^4. As a result, 8:1 and 1:4 blend ratio devices became the worst and best performing devices in this experimentation, respectively.

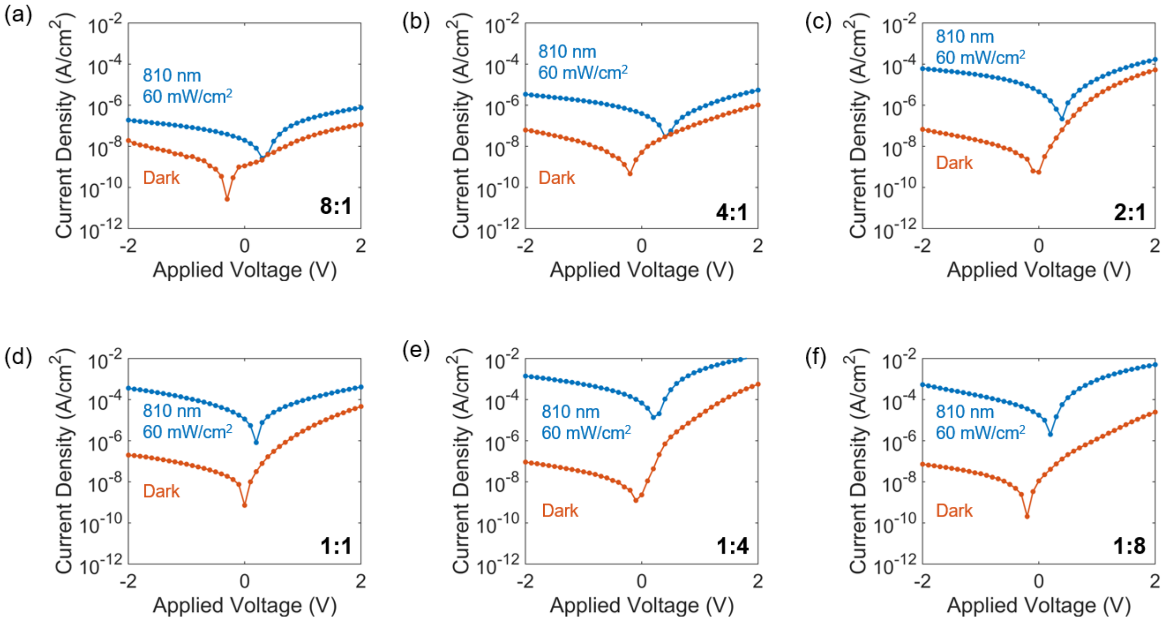

Fig. 3.6. (a - f) Current-voltage characteristics of the OPDs prepared with different blend ratios. The active area of the OPDs was 1 mm^2 and the measurements were performed with 810 nm NIR light with intensity of 60 mW/cm^2 [70].

After observing the current-voltage characteristics of the OPDs at the wavelength of 810 nm, the EQE, R, and D^*_{sh} of the devices were evaluated over the wavelength range of 500 nm to 900 nm. Note that the J_{photo}/J_{dark} ratio of 8:1 and 4:1 blend samples were so low that these parameters could not be measured reliably with our experimental setup, so 2:1, 1:1, 1:4 and 1:8 samples out of the total 6 samples were used for this comparison. The results of the EQE, R, and D^*_{sh} measurements are shown in Fig. 3.7. The 1:4 blend sample showed the highest EQE of 18%, R of 0.11 A/W, and D^*_{sh} of 2.1 × 10^{12} Jones at reverse bias of -0.5 V. These peak values were obtained at the NIR wavelength of 770 nm which coincided with the absorption peak of $8OH_2Pc$ indicating that the $8OH_2Pc$ material is the principal contributor of photo carrier generation in these bulk heterojunction devices.

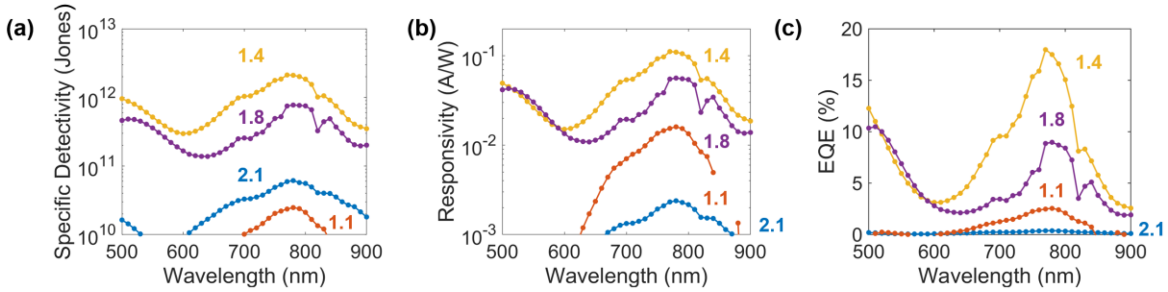

Fig. 3.7. (a) D^*_{sh}, (b) R, and (c) EQE spectra of the NIR photodetectors based on different blend ratios of $8OH_2Pc$:$PC_{61}BM$ [70].

It was interesting to note that the samples on both sides of 1.4 showed decreasing D^*_{sh}, responsivity, and EQE, although their relative positions were not the same as shown in Fig. 3.7. In terms of D^*_{sh}, sample 2:1 appeared to be better than sample 1:1, however, in terms of EQE, their positions were reversed. This discrepancy can be explained with the help of equations (2) and (4), showing that the EQE is dependent on R of the device and the absorption coefficient while the D^*_{sh} parameter is dependent on both R and J_{dark} of the device. As a low level of J_{dark} is a critical parameter for ensuring versatile operation and application of OPDs, D^*_{sh} is considered to be a better figure of merit for OPDs rather than EQE. As the sample 1:4 achieved the highest values in both of these performance metrics, it was undoubtedly the best performing OPD in this study.

3.3 Performance Analysis

As described in Chapter 1.2, the generation of photocurrent is the result of 4 steps: photon absorption with efficiency η_A, exciton diffusion where η_{ED} is the fraction of excitons reaching the DA interface, generated charge transfer exciton and the exciton dissociation at the DA interface with efficiency η_{CT}, and the collection of carriers at the electrodes with efficiency η_{CC}. To explain why the 1:4 blend sample achieved the champion performance, firstly, the absorption spectra of the blend films were considered. As shown in Fig. 3.2, it was evident that η_A was higher for the samples with higher concentration of $8OH_2Pc$. However, the 1:4 sample had a comparatively lower concentration of the light absorbing $8OH_2Pc$ material suggesting that η_A was not the underlying reason behind the improvement of performance. This assumption was confirmed by calculating the transmission adjusted EQE to compare the internal quantum efficiency across the samples where the relative positions of the blend samples were unchanged as shown in Fig. 3.8 [70]. So, even after accounting for the loss due to transmission, other samples could not overtake the 1:4 sample in performance.

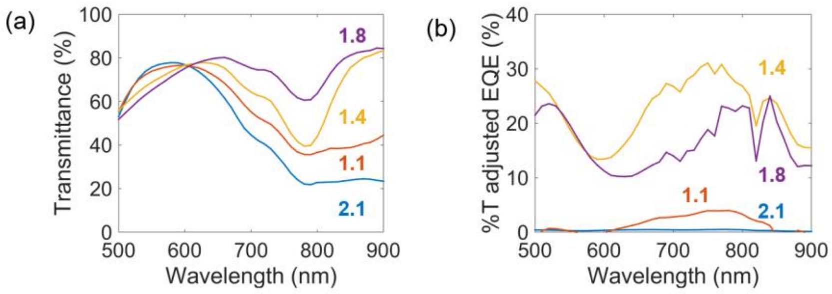

Fig. 3.8. (a) Transmittance and (b) Transmittance adjusted EQE spectra of different blend samples of $8OH_2Pc:PC_{61}BM$ [70].

Next, the change in η_{CC} was considered to be a possible reason behind the difference in performance. As the charge carrier mobilities (μ_{hole} and $\mu_{electron}$) of the blend films strongly influences how many photo-generated carriers can reach the electrodes without annihilation by trap sites which decreases mobility, η_{CC} is correlated with the carrier mobility. Therefore, the μ_{hole} and $\mu_{electron}$ of the blend samples were extracted using the MIS-CELIV method and they are summarized in Table I. The transient current outputs of the MIS devices are also shown in Fig. 3.9.

Table I. Extracted data from the transient current waveshapes of MIS devices prepared with $8OH_2Pc:PC_{61}BM$ bulk heterojunction samples.

Sample	|A| (V/s)	$\|j_0\|$ (A)	t_{2j0} (s)	t_{tr} (s)	ε_s	ε_i	d_s (cm)	d_i (cm)	μ (cm^2/Vs)
2:1 - hole	1500	1.1×10^{-6}	2.8×10^{-3}	3.7×10^{-3}	3	3.9	2.5×10^{-5}	1.0×10^{-5}	**7.8×10^{-8}**
2:1 – electron		8.3×10^{-7}	3.1×10^{-3}	4.1×10^{-3}					**6.4×10^{-8}**
1:1 – hole		9.0×10^{-7}	2.5×10^{-3}	3.3×10^{-3}					**9.8×10^{-8}**
1:1 – electron		7.9×10^{-7}	6.0×10^{-3}	8.0×10^{-3}					**1.7×10^{-8}**
1:4 – hole		1.2×10^{-6}	3.8×10^{-3}	5.1×10^{-3}					**4.3×10^{-8}**
1:4 – electron		9.2×10^{-7}	7.2×10^{-3}	9.6×10^{-3}					**1.2×10^{-8}**
1:8 – hole		1.2×10^{-6}	6.7×10^{-3}	8.9×10^{-3}					**1.4×10^{-8}**
1:8 – electron		9.0×10^{-7}	5.1×10^{-3}	6.8×10^{-3}					**2.4×10^{-8}**

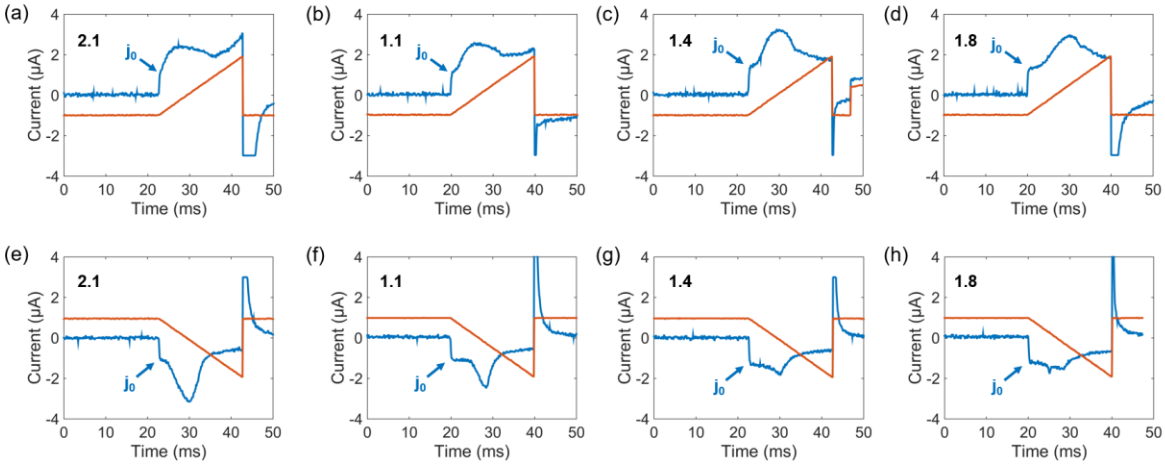

Fig. 3.9. (a-d) Transient current waveshapes for the evaluation of hole mobility. The samples were charged at -10 V and discharged at 20 V with a voltage rise rate of 1500 V/s. (e-h) Transient current waveshapes for the evaluation of electron mobility. The samples were charged at 10 V and discharged at -20 V with a voltage rise rate of -1500 V/s. The metal-insulator-semiconductor (MIS) system used in this study had the device structure of Si/SiO_2(100 nm)/Active layer(250 nm)/MoO_3(5 nm)/Au(50 nm) [70].

The hole and electron mobilities obtained by the MIS-CELIV method were in the order of 10^{-8} cm^2/Vs which is 2–4 orders of magnitude lower compared to other reported DA blends [27]. This low mobility was attributed to the edge-on orientation of the $8OH_2Pc$ molecules and polycrystalline nature of the active layer as evident by the out-of-plane XRD measurements. In case of discotic molecules, thin film deposited by spin-coating method commonly exhibits edge-on orientation which is not favorable for carrier transport in the vertical direction [31, 72]. Moreover, the polycrystalline nature of the thin film might have caused considerable grain boundary effect, resulting in poor carrier mobility for both hole and electron in the MIS devices. However, considering only the change in mobility, the hole and electron mobilities across the different samples were hardly changed on the order of 10^{-8} cm^2/Vs as shown in Table I so the efficiency of charge collection η_{CC} for each sample were almost the same. Thus, instead of η_A and η_{CC}, the high photocurrent of the 1:4 and 1:8 blend samples was attributed to the increase in η_{ED} and η_{CT} in the photoactive layer.

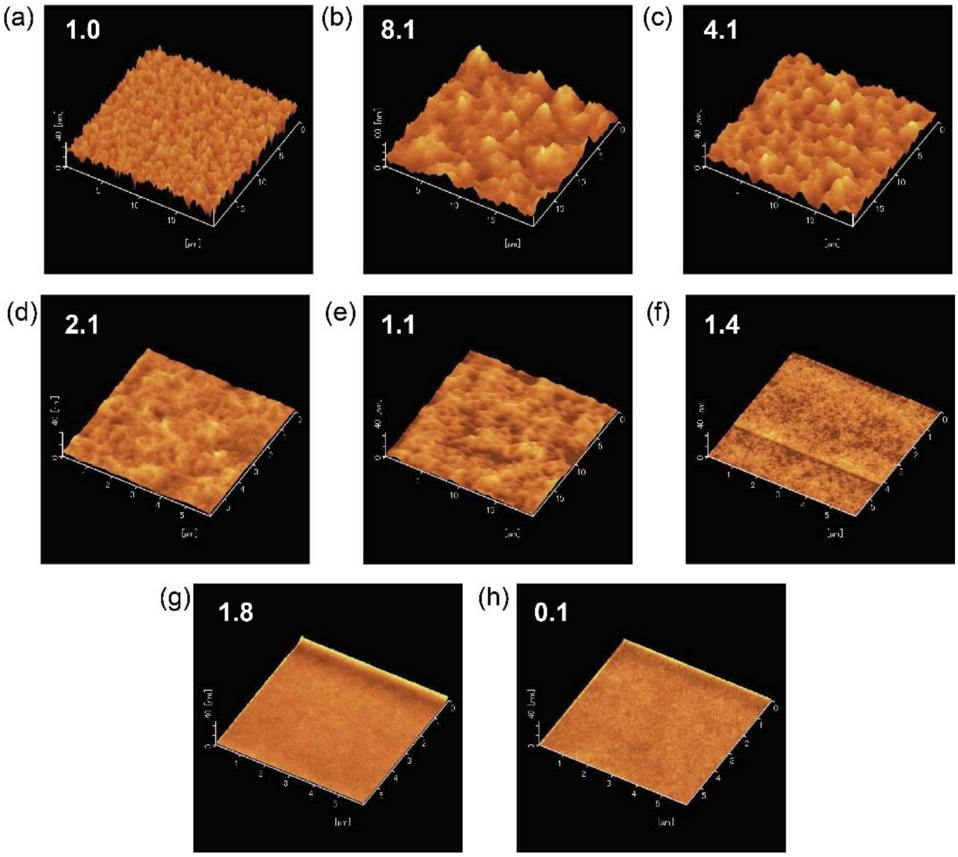

Fig. 3.10. (a-h) Surface morphology of the different blend samples observed with AFM in tapping mode [70].

To confirm for this assumption, the surface morphology of the thin films was observed with AFM in tapping mode as shown in Fig. 3.10. The neat film of $8OH_2Pc$, Fig. 3.10 (a), showed rough surface with clearly defined structures and that of neat $PC_{61}BM$, Fig. 3.10 (h), showed extremely smooth surface. This difference originated from the crystalline and amorphous nature of the materials as $8OH_2Pc$ tends to crystallize rapidly as the solvent evaporates during the spin-coating process. This results in distinguishable crystalline grains which could be observed with AFM. On the other hand, $PC_{61}BM$ forms amorphous thin film after spin coating and so no identifiable features could be observed with AFM.

In the case of the blend samples, they showed a steady decrease in surface roughness and increase in uniformity as the concentration of $PC_{61}BM$ increased. For reference, the RMS surface roughness of the 6 samples from 8:1 to 1:8 blend ratio were 9.3 nm, 6.1 nm, 1.3 nm, 2.1 nm, 0.58 nm, and 0.44 nm, respectively. Comparing the morphology of neat $8OH_2Pc$ with a lot of peak and valley structures to that of neat $PC_{61}BM$ with smooth surface, it could be concluded that the peaks and valleys on the surface morphology represented the relative size of grains inside the active layer. It could be estimated from the features in the AFM images that the grain size in the 8:1, 4:1 and 2:1 blend samples were in the μm order. However, the typical diffusion length of singlet exciton in organic semiconductors is in the order of 5–10 nm [73]. As a result, most of the excitons generated inside the grains of $8OH_2Pc$ recombined without being dissociated and contributing to the photo current. Then, as the relative content of $PC_{61}BM$ increased in the 1:1, 1:4 and 1:8 blend samples, the grain size of $8OH_2Pc$ decreased due to the nanophase separation inside the bulk heterojunction. In this case, more and more exciton pairs could reach the DA interface and the bulk heterojunction became more efficient in exciton dissociation leading to exponential increase in photo current. This increase continued until a limit was reached at the 1:4 blend sample beyond which the concentration of the light absorbing material, $8OH_2Pc$, became too low to generate enough excitons. Specifically, in the 1:8 blend sample, the relative content of $8OH_2Pc$ was only 11% which was reason that this sample could not absorb sufficient amount of the incident light for photo current output and thus the champion performance was observed at the 1:4 blend sample.

This performance at the blend ratio of 1:4 w/w of $8OH_2Pc$:$PC_{61}BM$ is noteworthy as reportedly the maximum photo current and EQE in bulk heterojunction OSCs were obtained at a ratio of approximately 1:1 w/w in polymer-based bulk heterojunction such as P3HT:$PC_{61}BM$ [74] and 2:1 w/w in small molecule-based bulk heterojunction such as $C6PcH_2$:$PC_{61}BM$ [75]. This might have resulted because of the compact π–π stacking and strong intermolecular force enabled by the presence of the oxygen atoms in the alkoxy chains of the $8OH_2Pc$ molecule. The crystalline nature of the spin-coated film as seen in the XRD patterns and AFM measurements and the slightly lower solubility of $8OH_2Pc$ compared to its alkyl counterpart $8H_2Pc$ support this assumption. As a result of this compact π–π stacking, the grain sizes in the bulk heterojunction tended to be much larger compared to other polymer- or small molecule-based bulk heterojunction even at a blend ratio of 1:1 w/w. Thus, a much higher concentration of amorphous $PC_{61}BM$ (80% by weight) was necessary to reduce the grain sizes to the optimum level and reach the maximum photocurrent, D^*_{sh}, and EQE values in the $8OH_2Pc$:$PC_{61}BM$ OPDs.

3.4 Summary of Chapter 3

In this chapter, the optical and electrical characteristics of $8OH_2Pc$:$PC_{61}BM$ based NIR OPDs were discussed. The champion devices were found at the blend ratio of 1:4 w/w and showed EQE of 18%, R of 0.11 A/W, and D^*_{sh} of 2.1×10^{12} Jones at 770 nm. From the observations of XRD spectra and AFM images, it was noted that $8OH_2Pc$ quickly crystallized after spin-coating and resulted in rough surface morphology and grain size of µm order in the bulk heterojunction active layer. With the increase in amorphous $PC_{61}BM$ content, the surface roughness and grain size were reduced, allowing photo generated exciton pairs to reach the DA interface efficiently and dissociate into free carriers. As a result, the best performance was observed at a relatively higher ratio of $PC_{61}BM$ compared to other contemporary reports. The results indicated the very significant role of bulk heterojunction condition on the performance of OPDs. It was also clear that the nature of the organic materials and their interaction influenced the morphology and crystalline order of the thin film ultimately impacting the performance of the organic devices.

Chapter 4

8H$_2$Pc:PC$_{61}$BM Near-infrared Organic Photodetectors

In this chapter, the optical and electrical characteristics of the organic photodetectors prepared with the blend of 8H$_2$Pc and PC$_{61}$BM are reported. The findings from the experimentation of 8OH$_2$Pc:PC$_{61}$BM OPDs were taken into consideration and the optimal bulk heterojunction condition for the 8H$_2$Pc:PC$_{61}$BM system was investigated. Discussion on the influence of liquid crystallinity in the bulk heterojunction condition and device performance is also presented based on XRD and AFM measurements. Finally, the devices were implemented on rigid glass substrates and their performance is compared based on the EQE, R, and D^*_{sh} figures of merit.

4.1 Optical Characteristics

As shown in Fig. 4.1, the neat 8H$_2$Pc material showed two peaks at 630 nm and 760 nm wavelength. The intensity of the peaks decreased in the blend samples with the increase in PC$_{61}$BM as it does not show any absorption in the mentioned wavelength region. Unlike the 8OH$_2$Pc:PC$_{61}$BM system, the 8H$_2$Pc:PC$_{61}$BM did not show any new peaks in the NIR region.

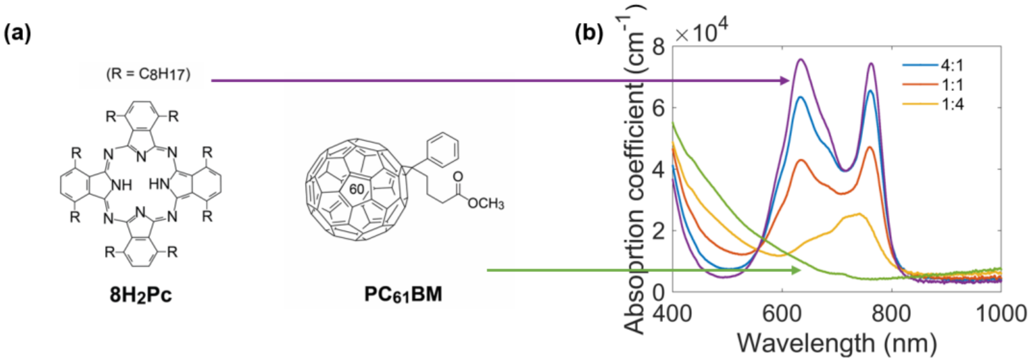

Fig. 4.1. (a) Chemical structures and (b) absorption spectra of the organic materials used in this study [69].

4.2 Electrical Characteristics

Fig. 4.2 shows the current-voltage characteristics of the 4:1, 1:1, and 1:4 samples under dark and illuminated by NIR light 740 nm of 3.2 mW/cm^2 conditions. Under dark condition, all the OPDs showed low reverse bias current density with the 4:1 sample showing the lowest 19 nA/cm^2 and the 1:1 and 1:4 samples showing 54 nA/cm^2 and 42 nA/cm^2 at -1 V, respectively.

However, the 1:1 sample showed the highest rectification ratio of 10^4 suggesting that good blocking contact was formed between the organic layer and electrodes which resulted in low carrier injection in the reverse bias but high carrier injection in the forward bias condition of the 1:1 sample. In addition, under illuminated condition, the highest reverse bias current was shown by the 1:1 sample with 0.56 mA/cm^2 which resulted in the champion R, EQE, and D^*_{sh} values of 0.2 A/W, 29%, and 1.3 × 10^{12} Jones, respectively.

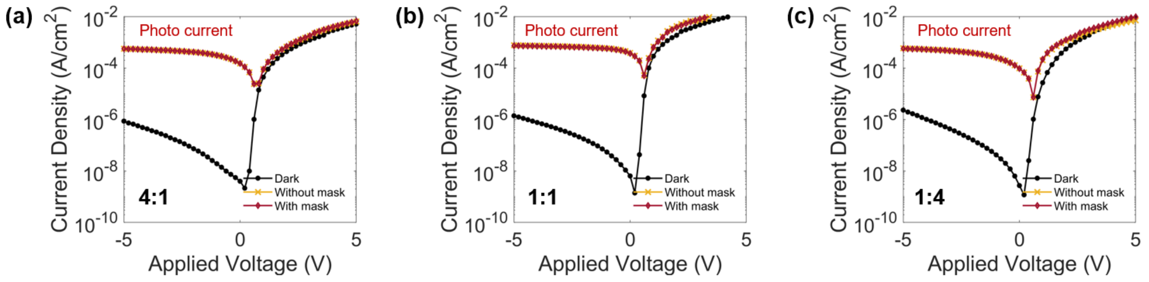

Fig. 4.2. Current-voltage characteristics of the (a) 4:1, (b) 1:1, and (c) 1:4 samples under dark and illuminated conditions. The device area was 16 mm^2 and the photo current was measured with and without using a shadow mask with an opening of 16 mm^2 and the incident light wavelength and intensity were 740 nm and 3.2 mW/cm^2, respectively [69].

In order to confirm whether excess exciton pairs generated outside the device area could enter the active area of the device and inflate the photo current, the photo current was measured with and without using a shadow mask with an opening of 16 mm^2. However, hardly any difference was observed between the measurements with and without the shadow mask as shown in Fig. 4.2. A relative difference of 4.1% in photo current was observed in the sample 1:1 while the other two samples showed less than 1% which was concluded to be negligible. It has been reported that the diffusion length of excitons in metal free phthalocyanine or organic bulk heterojunction is in the order of several nm and so it was surmised that almost all of the photo generated exciton pairs resulted in recombination outside of the device area and did not influence the photo current output [73, 76]. After confirming that the photo current measurement was accurate, the figures of merit of the OPDs were evaluated over the wavelength range of 500 nm to 900 nm.

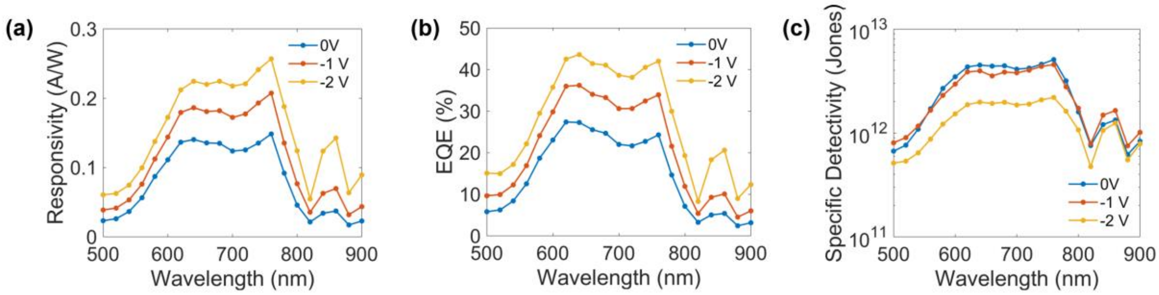

Fig. 4.3. (a) R, (b) EQE, and (c) D^*_{sh} spectra of the champion device at different reverse bias voltages.

As shown in Fig. 4.3, the R and EQE of the champion OPD improved upon increasing the reverse bias voltage as more photo-generated carriers could be collected by the electrodes and more photo current could be generated. However, it also meant that the corresponding dark current was increased and so the D^*_{sh} of the OPDs decreased in higher reverse bias. Considering this trade-off, the reverse bias voltage of -1 V chosen for evaluating the figures of merit of the OPDs. A complete comparison of the NIR OPDs at this reverse bias voltage of -1 V is provided in Table II which shows the superior performance of the 1:1 blend sample.

Table II. Figures of merit of the $8H_2Pc:PC_{61}BM$ NIR OPDs measured at 740 nm wavelength.

Blend ratio	**Rectification Ratio**	**EQE (%)**	**R (A/W)**	**D^*_{sh} (Jones)**
	-5 V to 5 V	At -1 V reverse bias		
4:1	6×10^3	16	0.1	1.2×10^{12}
1:1	1×10^4	29	0.2	1.3×10^{12}
1:4	4×10^3	13	0.08	6.8×10^{11}

Although the D^*_{sh} is a well reported and relatively easy to calculate figure of merit, its drawback is the assumption that the shot noise is the source of noise current in dark condition. This assumption results in overestimation of detectivity especially when there are other system-specific mechanisms contributing to the noise current such as flicker noise, or elements of static and dynamic disorder such as trapping/detrapping, generation/recombination mechanisms and so on [77]. As a consequence, to accurately assess the detectivity of an OPD, it is necessary to directly measure the NEP and extract the D^* according to equation (3). Figure 4.4 shows the measurement results for the champion OPD. At a bandwidth of 1 Hz, it was able to detect faint light of 740 nm down to 5 nW and so the NEP of the device was 5 nW/Hz$^{1/2}$. Note that the active area of the device was 0.16 cm^2, and so the power density was approximately 31 nW/cm^2. So, the specific detectivity of the OPD at 740 nm wavelength resulted in 2.5×10^8 Jones.

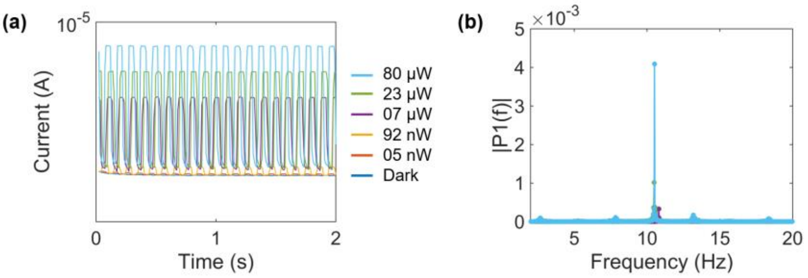

Fig. 4.4. (a) Transient photo current and (b) Fourier transform of the transient photo current of the photodetectors.

4.3 Performance Analysis

In our previous investigation of the OPDs fabricated with $8OH_2Pc:PC_{61}BM$ active layer, high photo current output was attributed to the increased efficiency of excitons reaching the DA interface and dissociating into free charge carriers to be eventually collected at the electrodes. These effects were made possible by smaller grain sizes and better intermixing of the materials at the blend ratio of 1:4 by weight where the best performance was observed [70]. The amorphous nature of $PC_{61}BM$ was helpful in suppressing to growth lager crystal grain of donor materials and so large DA interface area and small grain size was achieved at 80% $PC_{61}BM$ ratio. However, in the case of the $8H_2Pc:PC_{61}BM$ system, the relative content of $PC_{61}BM$ was less critical as the best performing OPD was achieved at 50% $PC_{61}BM$ ratio and all the OPDs showed markedly high EQE from 13% to 29%. This result suggested that the bulk heterojunction condition such as the grain size, crystalline order, intermixing condition, and surface morphology were favorable for good photo response across all the samples. In order to clarify and quantify these factors, the four process efficiencies of η_A, η_{CC}, η_{ED}, and η_{CT} were again considered. Similar to the previous observations, η_A was highest for the 4:1 sample but the champion performance was observed at the 1:1 $8H_2Pc:PC_{61}BM$ sample. So, it could be concluded that instead of η_A, other process efficiencies might have played a more important role. Next, to understand the change in η_{CC}, the charge carrier mobility in these bulk heterojunction samples were evaluated with the MIS-CELIV measurement technique. The results are summarized in the following table and the transient current waveshapes are shown in Fig. 4.5.

Table III. Extracted data from the transient current waveshapes of MIS devices prepared with 8H$_2$Pc:PC$_{61}$BM bulk heterojunction samples.

Sample	**|A| (V/s)**	**|j_0| (A)**	**t_{2j0} (s)**	**t_{tr} (s)**	**ε_s**	**ε_i**	**d_s (cm)**	**d_i (cm)**	**μ (cm^2/Vs)**
4:1 – hole	4000	9.6×10^{-7}	4.0×10^{-3}	5.1×10^{-3}	3	3.9	2.5×10^{-5}	1.0×10^{-5}	**1.6×10^{-8}**
4:1 – electron		-	-	-					-
1:1 – hole		1.3×10^{-6}	1.6×10^{-3}	2.1×10^{-3}					**9.4×10^{-8}**
1:1 – electron		-	-	-					-
1:4 – hole		2.1×10^{-6}	5.4×10^{-3}	6.9×10^{-3}					**8.6×10^{-9}**
1:4 – electron		2.1×10^{-6}	1.2×10^{-3}	1.5×10^{-3}					**1.8×10^{-7}**

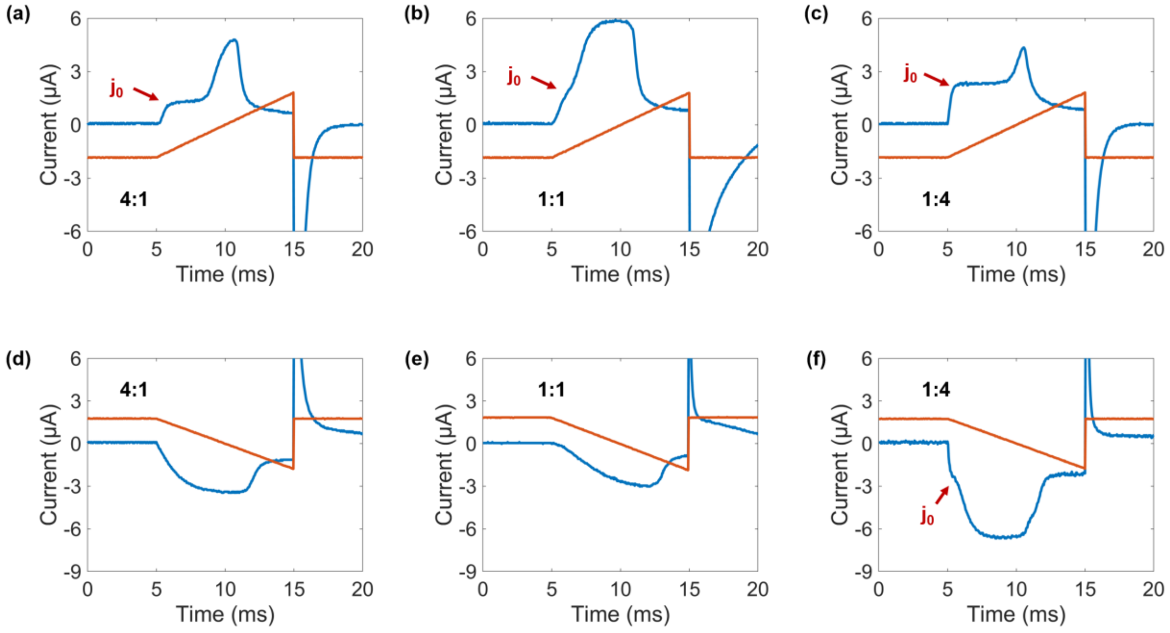

Fig. 4.5. (a-c) Transient current waveshapes for the evaluation of hole mobility. The samples were charged at -20 V and discharged at 20 V with a voltage rise rate of 4000 V/s. (d-f) Transient current waveshapes for the evaluation of electron mobility. The samples were charged at 20 V and discharged at -20 V with a voltage rise rate of -4000 V/s. The metal-insulator-semiconductor (MIS) system used in this study had the device structure of Si/SiO$_2$(100 nm)/Active layer(250 nm)/MoO$_3$(5 nm)/ Au(50 nm).

Comparing the hole mobility of different blend samples, it was observed that the 1:1 sample showed the highest mobility (9.4×10^{-8} cm^2/Vs) even compared to the 4:1 sample (1.6×10^{-8} cm^2/Vs). This result is interesting as it is expected that $8H_2Pc$ is the major hole transport material in the $8H_2Pc$:$PC_{61}BM$ system and so higher content of $8H_2Pc$ could show higher hole mobility. In this case, in the 1:1 sample, the presence of $PC_{61}BM$ might have helped by disrupting the random orientation of the disc-like molecules and creating a better vertical charge transport path between the electrodes which resulted in the better hole mobility. Due to this increased hole mobility, it was concluded that the η_{CC} for holes was comparatively better in the 1:1 sample.

Next, the electron mobility of the 1:4 sample was found to be 1.8×10^{-7} cm^2/Vs. However, the electron mobility of the 4:1 and 1:1 samples could not be extracted from the transient current waveshapes as these samples did not show any identifiable j_0 signal as shown in Fig. 4.5. It was assumed that the electron injection occurred in the $PC_{61}BM$ material in the MIS device. As the 4:1 and 1:4 samples had relatively low concentrations of $PC_{61}BM$, the electron injection was poor and so the current waveshapes did not show any j_0 signal. So, although the comparison of electron mobilities could not be confirmed, from the comparison of hole mobilities, it could be concluded that the 1:1 sample showed better performance due to the better η_{CC} for holes. In future, the electron mobility of all the samples can be compared by preparing MIS devices with a metallic electrode that has work function closer to the LUMO of $PC_{61}BM$. This will ensure that the electron injection takes place in all the samples and the j_0 signal can be identified.

Next, the comparisons of η_{ED} and η_{CT} were performed by the observations of XRD patterns and AFM images of the $8H_2Pc$:$PC_{61}BM$ thin films. First, as shown in Fig. 4.6 (a), neat $8H_2Pc$ material shows a peak at 4.7° corresponding to d-spacing 1.9 nm which coincides with the intercolumnar distance of the discotic molecules. The position of the XRD peak shown by the 4:1 sample was at the same position however the intensity of the peak was considerably lower. This suggested that the grains of $8H_2Pc$ in the bulk heterojunction film were isolated and pure similar to neat $8H_2Pc$ but without the long-range crystalline order which resulted in smaller grain size. Next, the XRD peaks shown by the 1:1 and 1:4 samples gradually shifted towards smaller angles and decreased in intensity suggesting that the grains became more mixed in nature, smaller in size, and the active layer condition became more amorphous-like with the increase of the ratio of the $PC_{61}BM$ material. A similar conclusion could be reached from the AFM images of the thin films (Fig. 4.7). The AFM image of neat $8H_2Pc$ exhibited clearly defined features on the film surface while that of the neat $PC_{61}BM$ showed extremely smooth and featureless surface, suggesting that the fiber-like texture observed on the surface of the 4:1, 1:1, and 1:4 samples originated from the pure $8H_2Pc$ grains. However, as the content of $PC_{61}BM$ increased, these features diminished, and the surface became smoother at the 1:4 sample. These observations suggested that at relatively higher concentration of $8H_2Pc$, the grains were isolated and pure while at higher concentration of $PC_{61}BM$, the grains became more and more mixed.

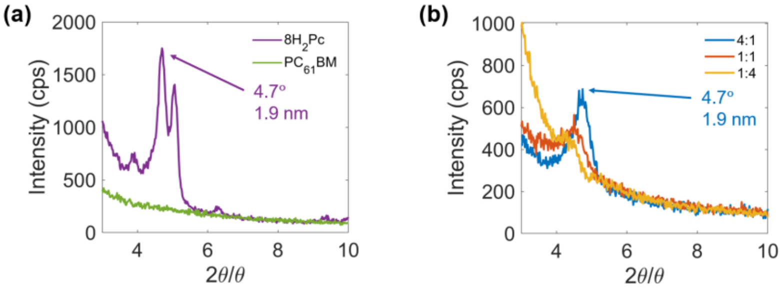

Fig. 4.6. XRD patterns of (a) neat $8H_2Pc$ and neat $PC_{61}BM$ and (b) different blend samples [69].

The AFM images also showed uniform and smooth surface morphology in all the samples with RMS surface roughness of 1.4 nm, 3 nm, and 1.3 nm for the 4:1, 1:1, and 1:4 samples, respectively. The fiber-like texture on the surface as shown in Fig. 4.7 (g) evidenced the thorough intermixing of $8H_2Pc$ and $PC_{61}BM$, creating grains of tens of nm-scale sizes and allowing the exciton pairs to reach the DA interface easily. It has been reported that the average diffusion length in organic materials is 5 nm to 10 nm, where the diffusion length of excitons in $PC_{61}BM$ is approximately 5 nm [78] and in metal free phthalocyanine it is approximately 7 nm [73]. However, depending on the nature of the material, the diffusion length can be longer as it has been reported that the exciton diffusion length of another LC phthalocyanine derivative, 1,4,8,11,15,18,22,25-octahexylphthalocyanine ($C6PcH_2$), is approximately 30 nm estimated by the photoluminescence quenching method [76]. As the size of the grains in the bulk heterojunction film in this study is of the same order of magnitude, higher number of photo generated exciton pairs could reach the DA interface, dissociate into free charge carriers, and ultimately reach the electrodes to produce high photo current output. In effect, the η_{ED} and η_{CT} became higher when the grain size became smaller and reached the order of 10s of nm. Note that, according the XRD patterns, the 1:4 sample showed the lowest peak, smallest grain size, and mixed grain condition. However, due the low content of the photo active $8H_2Pc$ material (only 20% by weight), the number of absorbed photons by this sample was less and consequently, the optimal condition for highest photon absorption, exciton pair generation, dissociation into free carriers, and carrier collection was reached in the 1:1 sample.

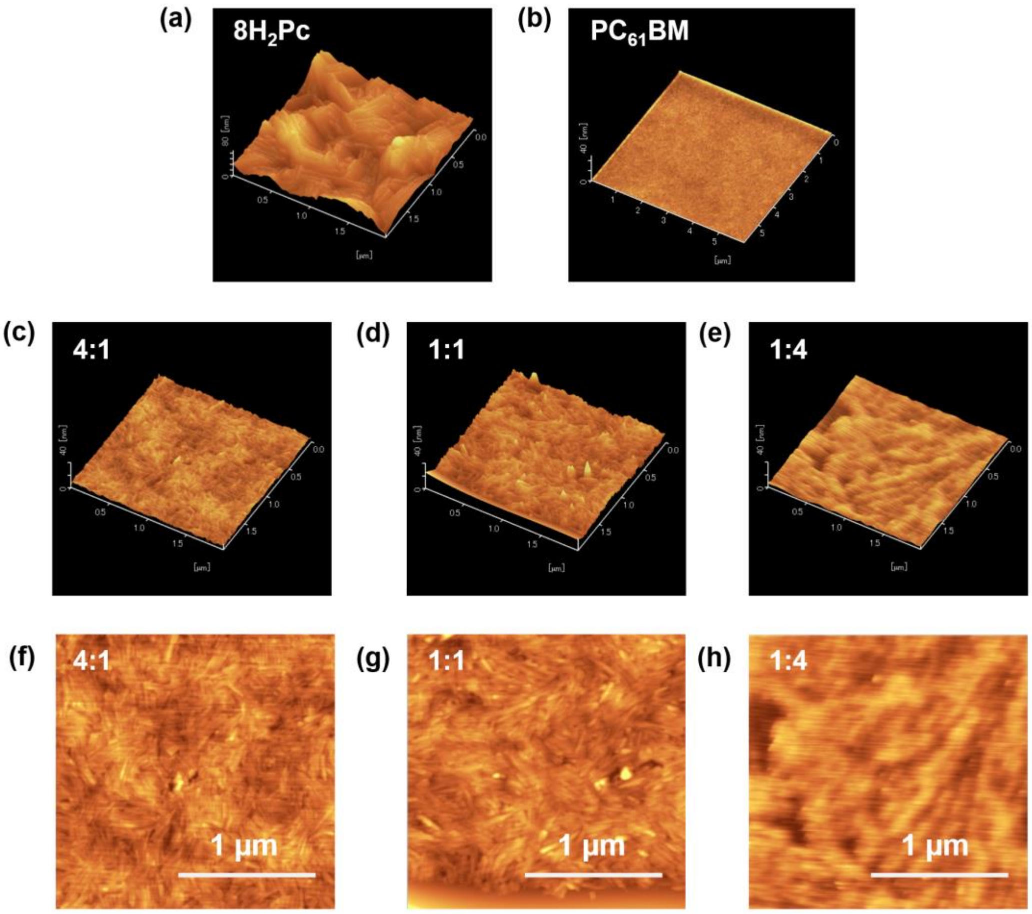

Fig. 4.7. Surface morphology of thin films prepared with (a) neat $8H_2Pc$, (b) neat $PC_{61}BM$, and (c-e) different blend samples observed with AFM in tapping mode, and (f-h) top view of the surface of the thin films with different blend ratios.

It was noted that regardless of the blend ratio, the $8H_2Pc$:$PC_{61}BM$ thin films were uniform with smooth surface morphology and small grain sizes as seen in the AFM images. These results are in high contrast to the conditions of the $8OH_2Pc$:$PC_{61}BM$ thin films which showed comparatively rough surface morphology and grain sizes in the order of µm. As the $8OH_2Pc$ material does not show any such mesophases, it quickly crystallized after spin-coating and created large crystal grains with long crystalline order. Although this long crystalline order may have been beneficial for the transport of charge carriers, large grain size and small area of the DA interface was found to be unfavorable for the generation of photo current. The weak intermolecular interaction and self-organizing nature of the LC $8H_2Pc$ material was thought to be useful in achieving large area of DA interface and grains of small size and good purity which ultimately resulted in better photo response.

Next, under illuminated condition, high open-circuit voltage of 0.7 V was consistent with the high work function difference between the PEDOT:PSS treated ITO electrode and the vacuum evaporated Al electrode. In addition, as shown in Fig. 4.8, the difference between the lowest unoccupied molecular orbital (LUMO) levels of the donor $8H_2Pc$ and acceptor $PC_{61}BM$ was approximately 0.4 eV. Considering the Coulomb potential based on an electron-hole distance of 1 nm and a dielectric constant of 3, the electrostatic attraction between an electron-hole pair at a donor-acceptor (DA) interface is estimated to be on the order of ∼0.5 eV [79]. As the LUMO-LUMO difference in the $8H_2Pc$:$PC_{61}BM$ system is very close to this limit, it is deemed that the energy level difference is sufficiently large for overcoming the binding energy and dissociate the excitons efficiently.

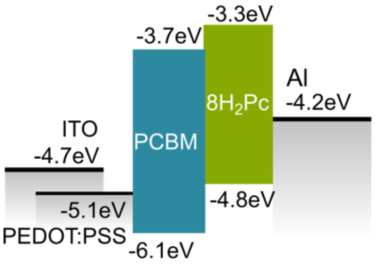

Fig. 4.8. Energy band diagram of the materials and electrodes in the $8H_2Pc$:$PC_{61}BM$ NIR OPD.

Finally, to explain the increase in J_{dark} with the increase of $PC_{61}BM$ content in the blend, the hole and electron injection was considered [80, 81]. The injection barrier for holes and electrons were calculated from the work functions of Al (-4.2eV) and PEDOT:PSS/ITO (-5.1eV) and the levels of highest occupied molecular orbital (HOMO), -6.1eV, and lowest unoccupied molecular orbital (LUMO), -3.7eV, of $PC_{61}BM$. So, in the reverse bias condition, it was calculated that the injection barrier for holes and electrons are 1.9 and 1.4 eV, respectively. As this barrier for electrons is lower than that for holes, the increasing J_{dark} of these NIR OPDs were attributed to the increase in charge injection into $PC_{61}BM$, particularly electron injection [70, 69]. As the relative content of $PC_{61}BM$ increased in the blend samples, the contact area of $PC_{61}BM$ and electrodes increased, making it easier for the electrons to be injected into the bulk heterojunction layer. As a result, the dark current in reverse bias condition increased with the increase of $PC_{61}BM$.

4.4 Conventional and Inverted Architecture

As shown in Fig. 4.9 (a), the current-voltage characteristics of the conventional OPDs showed comparatively high J_{dark} in the reverse bias condition. The J_{dark} showed continuous increase from 0 V onwards which was in high contrast to other state-of-the-art OPDs [82, 83, 4]. As the OPD was able to detect NIR light of 740 nm with J_{photo} in the order of 10^{-4} A/cm^2, therefore it was decided that the exciton pair generation, dissociation, and photo carrier generation in the active layer was not a problem. But due to the high J_{dark}, the detectivity D^*_{sh} was limited to 1.3×10^{12} Jones at -1 V bias.

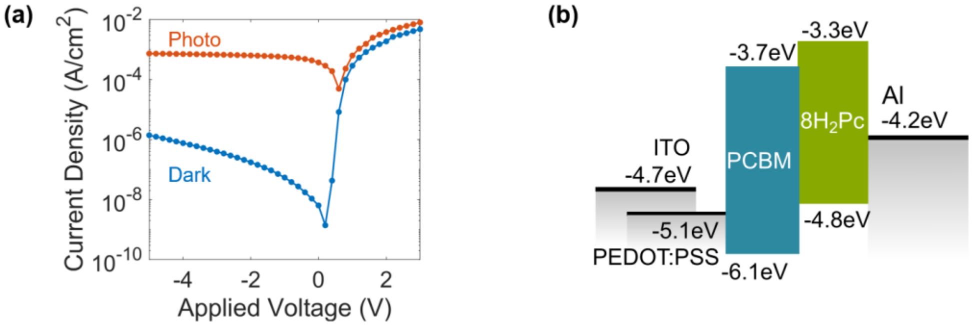

Figure 4.9. (a) Current-voltage characteristics and (b) energy level diagram of the conventional OPD. Measurements were performed with 740 nm light at intensity of 3.2 mW/cm^2.

To improve the performance of the OPD, it was evident that the dark current level needed to be reduced. After considering the energy band diagram of the conventional OPDs as shown in Fig. 4.9 (b), it was supposed that the Al/organic layer interface barrier was not enough to block injection of holes in the reverse bias condition. So, it became necessary to investigate a different device structure with a different electrode/organic layer interface. For this purpose, the inverted OPD structure was implemented, and the performances were compared. Figure 4.10 (a) shows the immediate improvement in dark current in the inverted OPDs. Compared to the conventional OPDs, the inverted OPDs showed lower J_{dark} levels by more than 2 orders of magnitude (from 1.4 µA/cm^2 to 9.2 nA/cm^2 at -5 V bias). Moreover, the J_{dark} remained roughly constant over the reverse bias range of 0 V to -5 V suggesting very good blocking contact between the organic layer and the electrodes. This blocking contact was achieved by the modification of the ITO surface by the PEIE interlayer which lowered the work function of ITO by nearly 1 eV [37, 84]. In addition, the function of the MoO_3 interlayer was to align the energy levels at the interface of the organic layer and Au electrode [85]. By inserting this layer, the energy level shift of the organic $PC_{61}BM$ could be prevented and a large electron injection barrier of 1.4 eV could be realized. Fig. 4.10 (b) shows the energy level diagram of the functional materials in the inverted photodiode [86].

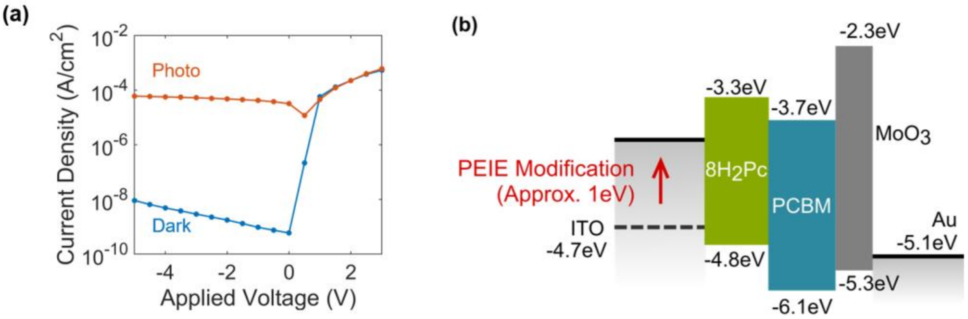

Figure 4.10. (a) Current-voltage characteristics and (b) energy level diagram of the inverted OPD. Measurements were performed with 740 nm light at intensity of 19.7 mW/cm^2.

After confirming the improved performance of the inverted OPDs, the EQE, R and D^*_{sh} were measured over the wavelength range of 500 nm to 900 nm. The results are shown in the following figure.

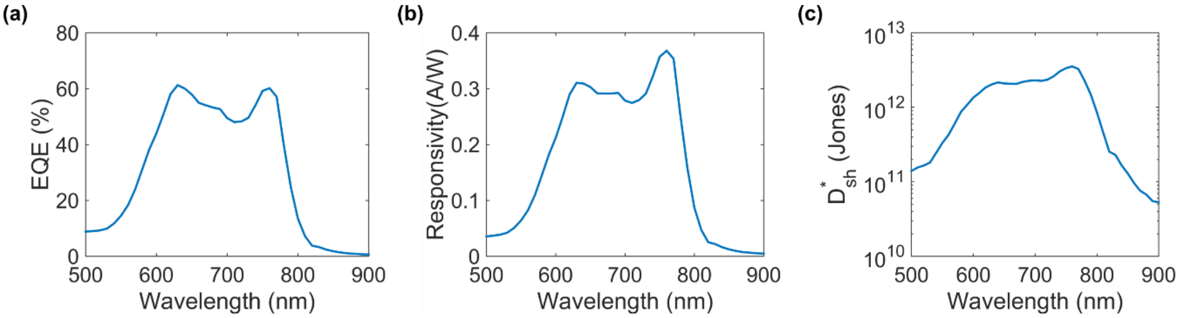

Figure 4.11. (a) EQE, (b) R and (c) D^*_{sh} of the best performing inverted PD. The active area of the diodes was 1 mm^2 and the bias voltage was -1 V.

The measurements showed very good EQE, with maximum value of 61.3% at 630 nm and 60% at 760 nm as shown in Fig. 4.11 (a). The R was also impressive with maximum value of 0.37A/W at 760nm and 0.32 A/W at 740 nm as shown in Fig. 4.10 (b). As it is evident from eqn. (2) and (4), D^*_{sh} depends significantly on the dark current rather than EQE. Therefore, although the value of EQE improved with the increase in bias voltage, the value of D^*_{sh} of the NIR OPDs actually decreased with bias voltage. At 0 V bias, the dark current was minimum and so the calculated D^*_{sh} had the maximum value of 1.1×10^{13} Jones. As these OPDs are intended for use in the photoconductive mode, the D^*_{sh} at -1 V bias was also calculated and it was found to be 3×10^{12} Jones.

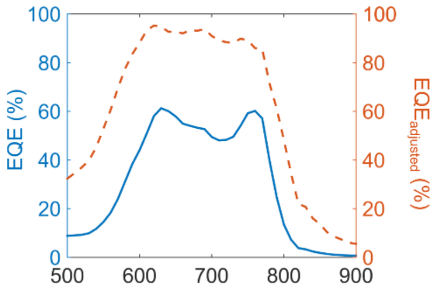

Figure 4.12. Comparison of EQE and $EQE_{adjusted}$ spectra of the inverted OPD at reverse bias voltage of -1 V.

To understand the internal photo carrier generation efficiency of the active material, the transmittance data was used to calculate the $EQE_{adjusted}$ over the wavelength region of 500 nm to 900 nm. Figure 4.12 shows that the $EQE_{adjusted}$ reached 95% at 620 nm and stays well above 80% up to 770 nm. Thus, it was concluded that within this spectrum range, the internal carrier generation efficiency was nearly unity in the case of these OPDs and so the value of EQE was close to the maximum limit with the current device configuration.

4.5 Effect of Thermal Annealing

The process of thermal annealing has been widely reported in different fields of devices including organic transistors, photodetectors, and solar cells. In many cases, the performance of certain devices has been reported to be better due to change in molecular orientation, phase separation, aggregation formation, or optimization of the crystallite size [29, 87, 28]. Thus, the effects of annealing on the performance of neat $8H_2Pc$ photodetectors were investigated, and the investigation results are discussed in this chapter.

4.5.1 Neat $8H_2Pc$ Thin Films

Figure 4.13 shows the absorption coefficient and XRD spectra of as coated and annealed samples of neat $8H_2Pc$ thin films. The TA140-Slow and TA140-Rapid samples correspond to the annealing process as described in Chapter 2.2.2. Firstly, peak positions of as coated and annealed films in out-of-plane XRD were the same at 4.7° which corresponds to d-spacing of 19 Å between columns. This strongly indicated that the crystal structure is not changed. However, peak intensity was signification changed, which indicated that the columnar orientation was changed. The sharp peak in the in-plane XRD pattern of TA140-Slow indicated the orientation of the molecules in the thin film was face-on, while the sharp peak of the as coated sample in the out-of-plane XRD pattern indicated that the orientation was edge-on. The effect of this change in molecular orientation was shown in the absorption spectra as the peak at 760 nm gradually decreased in intensity from as coated to TA140-Rapid and finally to TA140-Slow samples. The results indicate that the intensity of 630 nm was increasing on the film with face-on molecular orientation, on the other hand, the intensity of 760 nm was increasing on the film with edge-on orientation.

The in-plane XRD spectra shown in Fig. 4.13 (b) was also used to evaluate the degree of face-on orientation as defined in Chapter 1.6. In this case, the intensity of the TA140-Slow sample (416 cps) was considered to have degree of face-on orientation equal to 1. Relative to this value, the TA140-Rapid and as coated samples showed degrees of face-on orientation equal to 0.47 and 0.14, respectively. The corresponding values of peak intensity were 196 cps and 59 cps, respectively.

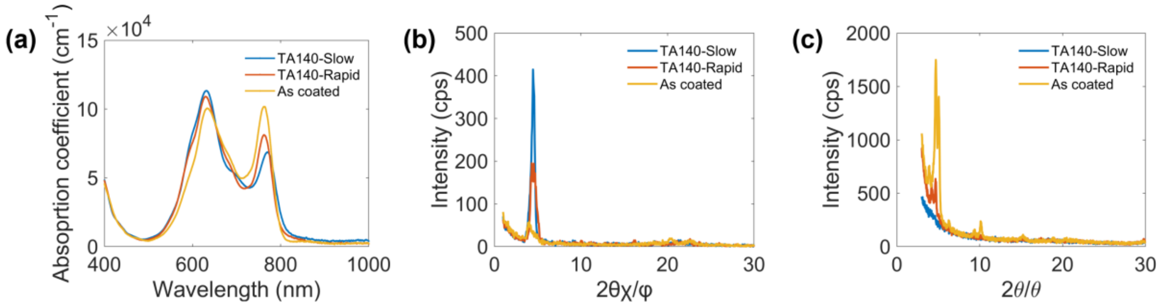

Fig. 4.13. (a) Absorption coefficient, (b) in-plane and (c) out-of-plane XRD spectra of as coated and annealed samples.

This effect was also confirmed by checking the POM images as shown in Fig. 4.14. The as coated sample showed grain-like texture with much retardation while the TA140-Slow and TA140-Rapid samples showed dark optical texture indicative of face-on oriented molecules [31, 88]. The POM image of the TA140-Slow sample (Fig. 4.14 (b)) shows completely dark texture at the right side and some retardation at the left side. As this sample was slowly cooled, the nucleus of the face-on oriented molecules originated somewhere in the middle of the sample and reached this edge of the domain after spreading outwards. This completely dark texture on the right side suggested that the degree of face-on orientation was higher in the TA140-Slow sample compared to the mostly dark texture of the TA140-Rapid one (Fig. 4. 14 (c)).

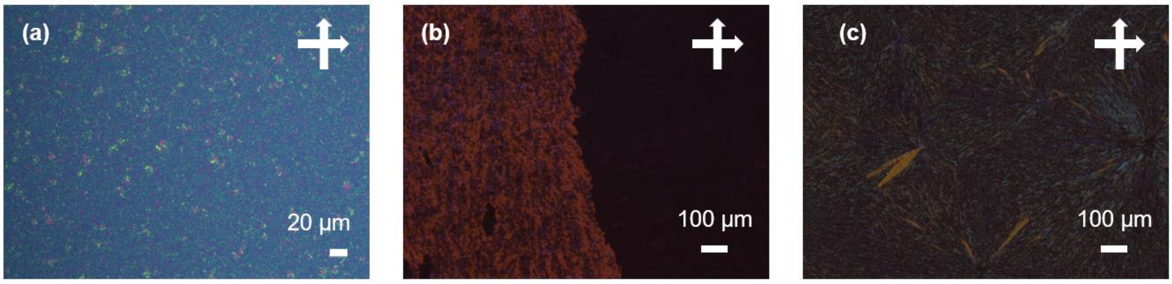

Fig. 4.14. POM images of (a) as coated, (b) TA140-Slow, and (b) TA140-Rapid samples prepared with neat $8H_2Pc$ material.

These results suggested that the molecules in the spin-coated thin film of $8H_2Pc$ tend to be in edge-on orientation facing in random direction along the surface of the substrate. Due to the presence of the liquid crystalline mesophase, it was possible to reorient the direction of the molecules to face-on orientation which resulted in the dark texture. As the photodetector prepared in this study is a vertical device, it was presumed that this change in orientation from edge-on to face-on might be beneficial to the performance of the device by transporting the carriers in the vertical direction through the core of the $8H_2Pc$ material. To validate this presumption, photodetectors with as coated, TA140-Rapid, and TA140-Slow thin films were prepared with a device structure as shown in Fig. 4.15 (a). The current-voltage characteristics under dark condition clearly illustrates that the annealed samples showed better diode performance with higher rectification ratio. This better performance also was reflected in the output current under illuminated condition where the TA140-Slow sample showed the highest J_{photo} of 150 µA/cm^2, and the as coated sample showing the lowest J_{photo} of 2.5 µA/cm^2 at -10 V reverse bias.

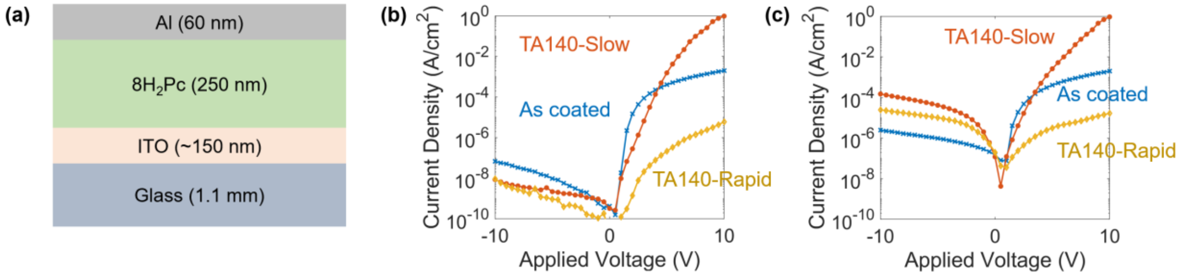

Fig. 4.15. (a) Schematic illustration of the device and current-voltage characteristics of the device under (b) dark and (c) illuminated condition. The devices were illuminated with NIR light of 740 nm wavelength at 1.4 mW/cm^2.

For a comprehensive comparison of these devices, the figures of merit of these devices are summarized in the following table.

Table IV. Summary of figures of merit of photodetectors with as coated and annealed active layer of neat $8H_2Pc$.

Sample name	**Rectification ratio**	**J_{photo}/J_{dark}**	**R (mA/W)**	**EQE (%)**	**D^*_{sh} (Jones)**
	at ±10 V	at -10 V			
As coated	3×10^4	36.3	1.7	0.003	1.2×10^{10}
TA140-Slow	1.1×10^8	1.7×10^4	106.9	0.2	2.0×10^{12}
TA140-Rapid	6.4×10^2	2.6×10^3	17.7	0.03	3.2×10^{11}

In addition to the molecular orientation, the change in dielectric constant of the $8H_2Pc$ material was also investigated as shown in Fig. 4.16. It was observed that the at isotropic phase temperature of 160°C, the ε_r at 10 kHz was equal to 2.66. As the sample was cooled slowly at a rate of 4°C/min, the ε_r gradually increased to 2.78 at 70°C. Finally, when the sample at the crystalline phase temperature of 34°C and the disc-like molecules were in the face-on orientation, the ε_r was evaluated at 3. The value of ε_r at crystalline phase was unchanged at 3 even when the sample was rapidly cooled from 160°C to 20°C.

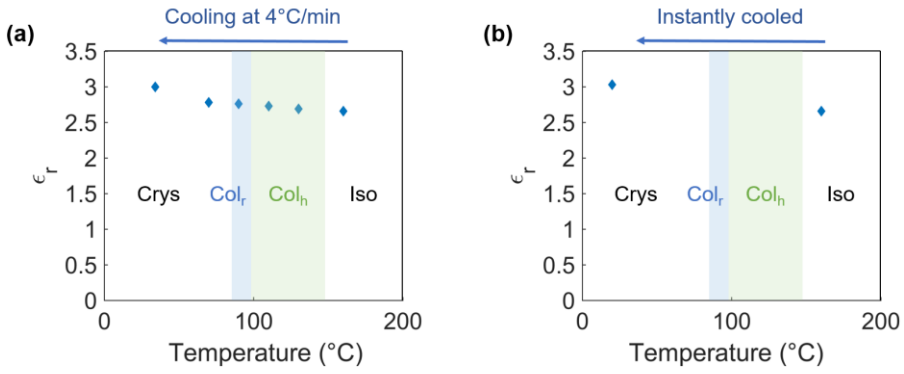

Fig. 4.16 Change in dielectric constant of $8H_2Pc$ at 10 kHz when the sample was (a) cooled at a rate of 4°C/min and (b) instantly cooled.

This result suggested that there was no significant change in the dielectric constant of the neat $8H_2Pc$ material regardless of the orientation of the molecules being random in the isotropic phase or face-on in the crystalline phase. It was concluded that this lack of change was observed as there is no strong dipolar moment present in the disc-like $8H_2Pc$ molecules. In addition, as there was no significant change in ε_r in different molecular orientations, it was concluded that the efficiency of exciton pair dissociation was not significantly different in as coated and annealed samples.

4.5.2 $8H_2Pc:PC_{61}BM$ Bulk Heterojunction Thin Films

The condition of the bulk heterojunction thin film differs considerably from that of the neat thin films. Thus, the effect of thermal annealing on bulk heterojunction films was also investigated by varying the annealing duration and rate of cooling. These films were prepared with the blend ratio of the champion OPDs e.g., 1:1 w/w of $8H_2Pc:PC_{61}BM$. Furthermore, 3 different annealing temperature was chosen: 50°C, 90°C, and 140°C. As shown in Fig. 4.17, when annealing at 50°C, no appreciable change was observed in optical texture and absorption spectra regardless of the time duration of annealing and the rate of cooling. It was concluded that the molecular orientation of the $8H_2Pc$ molecules were not changed by this annealing process.

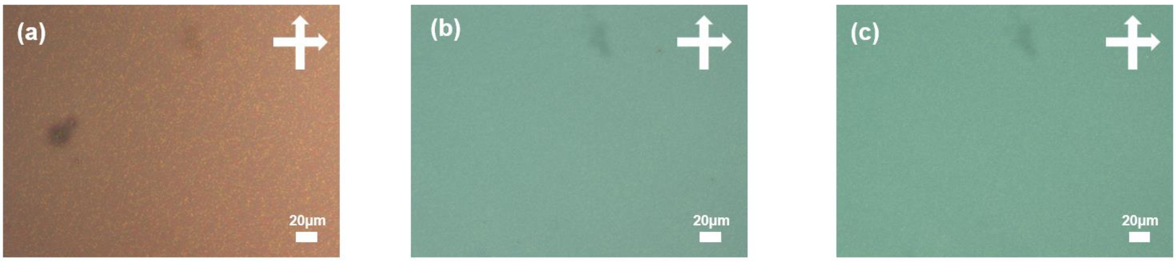

Fig. 4.17. POM images of (a) as coated, (b) TA50-Slow, and (b) TA50-Rapid samples prepared with $8H_2Pc:PC_{61}BM$ blend samples in 1:1 ratio.

Next, the bulk heterojunction samples were annealed at 90°C which in the Col_r phase temperature of neat $8H_2Pc$ material. The TA90-Slow sample was annealed for 30 mins and cooled down to room temperature at a rate of 3°C/min and it showed obvious phase separation between the $8H_2Pc$ and $PC_{61}BM$ materials. However, the TA90-Rapid sample was annealed for 1 min and cooled down rapidly to room temperature and it did not show any significant difference from the as coated sample. Thus, it was concluded that long duration thermal annealing at the Col_r phase temperature is necessary to change the condition of the thin film as shown in Fig. 4.18.

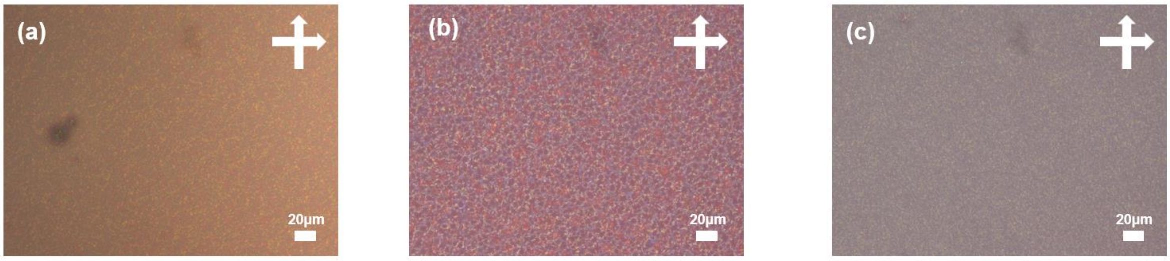

Fig. 4.18. POM images of (a) as coated, (b) TA90-Slow, and (b) TA90-Rapid samples prepared with $8H_2Pc:PC_{61}BM$ blend samples in 1:1 ratio.

Finally, the bulk heterojunction samples were annealed at 140°C which is the Col_h phase temperature of neat $8H_2Pc$ material. The TA140-Slow sample was annealed for 30 mins and cooled down to room temperature at a rate of 3°C/min while the TA140-Rapid sample was annealed for 1 min and cooled down rapidly to room temperature. Contrary to the samples annealed at 90°C, both TA140-Slow and TA140-Rapid samples showed phase separation and change in absorption spectra. The grain size of the phase separated materials were quite different in the samples underlying the significance of time duration of the annealing process.

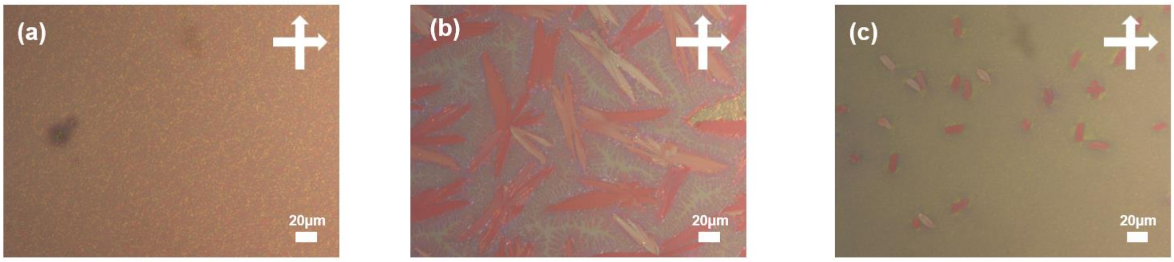

Fig. 4.19. POM images of (a) as coated, (b) TA140-Slow, and (b) TA140-Rapid samples prepared with $8H_2Pc:PC_{61}BM$ blend samples in 1:1 ratio.

The conjectures about change in molecular orientation were confirmed by evaluating the absorption spectra of the sample before and after thermal annealing. As shown in Fig. 4.20, the relative intensity of the peak at 760 nm coincides with the conclusions made from the POM textures. The intensity of the peak is completely unchanged in the TA50-Slow and TA50-Rapid samples suggesting no change in molecular orientation. On the other hand, the reduced intensity of the peak in the TA90-Slow sample suggested that the molecular orientation was changed from edge-on to face-on only in this sample but not in the TA90-Rapid one. Finally, significant change in the intensity of the same peak in TA140-Slow sample indicated that the degree of change of molecular orientation from edge-on to face-on was highest in this sample compared to all the others. The changes in this peak strength indicated that the growth grains after thermal annealing at 90°C and 140°C are in the face-on molecular orientation.

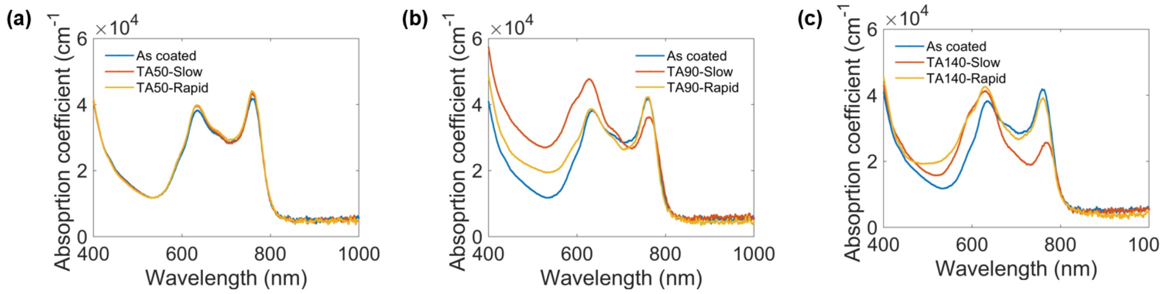

Fig. 4.20. Comparison of absorption spectra of 1:1 blend samples of $8H_2Pc$:$PC_{61}BM$ annealed at different temperatures.

Note that the change in grain size for annealing at 90°C and 140°C was significantly different. To clarify the reason behind this difference, the DSC of the $8H_2Pc$:$PC_{61}BM$ blend material was measured as shown in Fig. 4.21 (a). The result showed that the melting point of the blend material was reduced to 137°C from 149°C of the neat $8H_2Pc$ material. As a result, the temperature range of the LC mesophase was reduced and the annealing temperature of 140°C was found to be in the isotropic phase. From these observations, it could be concluded that thermal annealing at isotropic phase temperature creates large area grains in the order of 10s of µm for both short and long duration annealing. On the other hand, thermal annealing at LC temperature creates much smaller grains whose size can be controlled by modulating the annealing duration and cooling rate.

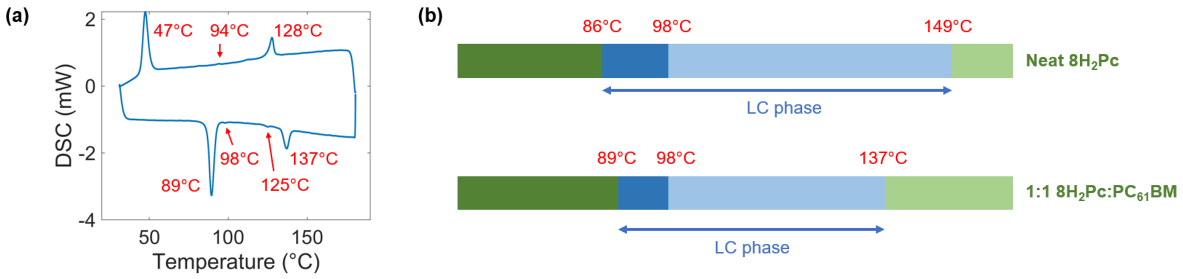

Fig. 4.21. (a) DSC thermogram of the $8H_2Pc$:$PC_{61}BM$ blend material with ratio of 1:1 w/w and (b) comparison of the phase transition temperatures of neat $8H_2Pc$ and $8H_2Pc$:$PC_{61}BM$ materials.

4.6 Summary of Chapter 4

In this chapter, the optical and electrical characteristics of $8H_2Pc:PC_{61}BM$ based NIR OPDs were discussed with respect to their bulk heterojunction condition. The champion device was found at the blend ratio of 1:1 w/w in the inverted architecture and it showed EQE of 60%, R of 0.4 A/W, and D^*_{sh} of 3×10^{12} Jones at the NIR wavelength of 760 nm. The performance of these OPDs were superior to that of $8OH_2Pc:PC_{61}BM$ ones which was attributed to the increase in hole mobility, smooth surface morphology, better intermixing condition of the blend materials, and creation of small grains whose size was in the order of tens of nm in the bulk heterojunction active layer. The weak intermolecular interaction and self-organizing nature of the liquid crystalline $8H_2Pc$ material was accredited for achieving these beneficial effects. As a result of the good intermixed bulk heterojunction condition, large DA interface area and small grains were possible at the blend ratio of 1:1 w/w in $8H_2Pc:PC_{61}BM$ contrast to 1:4 w/w in $8OH_2Pc:PC_{61}BM$. Furthermore, it was observed that by annealing the spin-coated thin films of neat $8H_2Pc$ and $8H_2Pc:PC_{61}BM$ bulk heterojunction at liquid crystalline temperature with a sacrificial polymer layer, the orientation of the $8H_2Pc$ molecules could be changed from edge-on to face-on orientation. After this change in molecular orientation, the performance of photodetectors improved but no significant change was observed in the dielectric constant of the $8H_2Pc$ material. Thus, this improvement was attributed to the better charge carrier transport in the vertical direction. The thermal annealing effect was investigated in both neat and bulk heterojunction thin films and the improved photodetector performance of the neat $8H_2Pc$ based devices suggesting the advantage of using liquid crystalline materials in photodetector applications. Finally, by annealing the bulk heterojunction sample at LC phase and isotropic phase temperatures, it was found that annealing at LC phase temperature offered more control over the phase separation and change in grain size.

Chapter 5

Photodetectors for Biomedical Application

5.1 Introduction to Photoplethysmography

Photoplethysmography, commonly abbreviated as PPG, is a method to measure the volumetric variations of blood circulation using NIR light to derive different health parameters. it is an uncomplicated and inexpensive optical measurement method that is often used for the purpose of monitoring heartbeat rate [89]. The technique utilizes the fact that the arterial blood of the human body changes in proportion to the pumping action of the heart. As NIR light is absorbed by the arterial blood, the change in its volume will also affect the portion of the incident light being absorbed, reflected, and transmitted. Thus, a NIR photodetector can detect this change in reflection or transmission of light and its output can be used to acquire information regarding different heart activities and conditions. With high resolution data and signal processing, it is possible to extract valuable information about the cardiovascular system and different diseases or health risks [90]. Depending on the principle of collecting this PPG data, PPG sensors can be divided into two types: reflection type and transmission type.

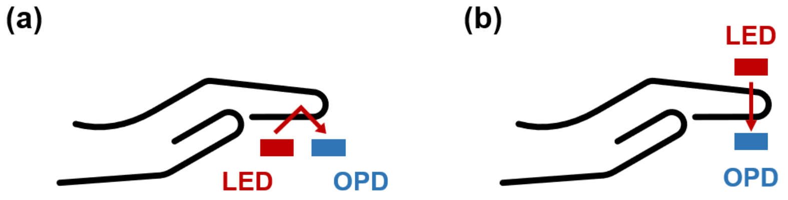

Fig. 5.1. Schematic illustration of (a) reflection type and (b) transmission type PPG sensor.

A reflection type PPG sensor is shown in Fig. 5.1 (a) where the NIR LED and the NIR OPD are arranged on the same side of the tissue, in this case, the index finger. The LED transmits NIR light which is reflected by the blood vessels in the finger and the change is detected by the NIR OPD. On the other hand, a transmission type PPG sensor is shown in Fig. 5.1 (b) where the LED and OPD are arranged on opposite sides of the index finger. In this case, the NIR light transmitted by the LED passes through the blood vessels in the index finger and the transmitted light is detected by the OPD. Comparative study on the accuracy of signal and comfort of use of these two types of PPG sensors reported that the reflection type PPG sensor was more comfortable to use for long periods of time while also showing better results if it could be positioned directly on the vein [91]. If the sensor was positioned outside the vein, the observed signal contained much noise and had lower amplitude. To circumvent this issue, it was mentioned that expensive commercial fitness bracelets use more than one LED sources arranged around a large-area photodetector. It was also reported that the accuracy of signal of the transmission type PPG sensor depends on the thickness of the tissue. For this reason, the signals obtained through the little finger and ear lobe were considered to be very good. However, the PPG sensor positioned on the ear lobe was the least comfortable to use as the subject could not move their head while the measurement was being performed.

Due to this dependence on tissue thickness, transmission type PPG sensors often make use of tissue compression mechanisms such as a finger clip. Such tissue compression allows the incident light to penetrate deeper into the tissue and allows the OPD to pick up stronger transmission signals. While NIR light is well-known for its ability to penetrating deep into the soft tissues, visible light cannot reach such depths due to its stronger absorption coefficient in biological tissues [92]. However, by using the tissue compression technique, green light can also be used to probe the blood volume changes in dermal arterioles and effectively monitor the PPG signal [93]. Thus, depending on the placement and operation mode of the PPG measurement device, different sources of light can be utilized.

Although the primary use of the PPG technology is in clinical and medical diagnosis field, it has gained popularity as an alternative heart rate monitoring technique for consumer applications. This increase was driven mainly by the simplicity of the operation of the equipment, the wearing comfortability for the consumers or users, and the cost effectiveness [94]. A popular example is the Apple Watch which contains a compact PPG system and can track the heartbeat rate of the user from the change in blood volume in the wrist [95]. As such consumer products become more affordable and the health consciousness of people increase, the demand and utility of PPG and other health monitoring methods can be expected to continue to grow. In this chapter, the air stability and reliability, response speed, linearity, and flexibility of $8H_2Pc:PC_{61}BM$ NIR OPDs were investigated in order to use these devices for biomedical application.

5.2 Air Stability and Reliability

One of the main challenges of organic devices is its poor stability when exposed to ambient air and humidity. Nonetheless, in practical applications, a device must exhibit stable and reliable performance for a reasonable period of time or until its utility is no longer necessary. Thus, it is paramount that the air stability of any device is evaluated and if instability is observed, proper measures are taken to confirm stable performance.

5.2.1 Conventional Photodiode

In order to investigate the mechanism of performance degradation and prevention methods, conventional photodiodes were prepared and evaluated each day after fabrication. The samples were at first measured within one hour of their fabrication, shown as “Fab day” in the following figures. After this measurement, the samples were placed inside a small desiccator and the inside of the desiccator was kept at a vacuum of -20 kPa. The samples were then taken out of the desiccator each time for measurement and then placed back inside the desiccator until the next measurement. These measurement data were collected over a span of 5 days, and they are shown as Fab day to Fab day+4 in Fig. 5.2.

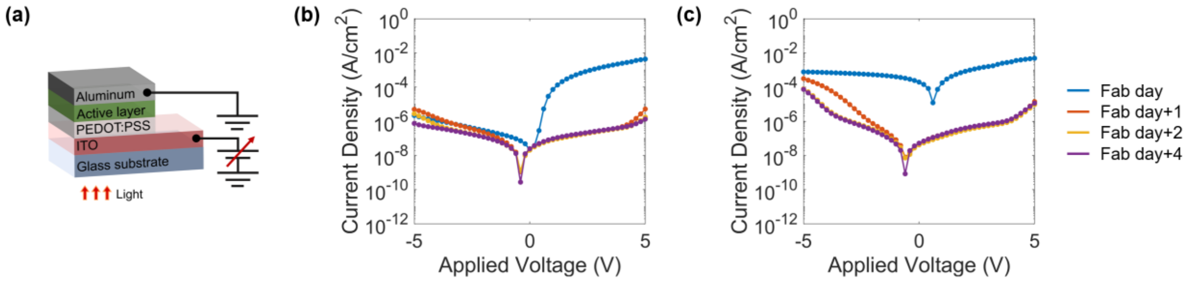

Fig. 5.2. (a) Schematic illustration of the device, and current-voltage characteristics of the device under (b) dark and (c) illuminated condition over a 5-day period.

The photodetectors showed low J_{dark} and high J_{photo} in the reverse bias condition on Fab day. However, within 24 hours, the J_{photo} deceased significantly and after 48 hours, nearly no J_{photo} could be observed at low reverse bias condition. This suggested that the photo carrier generation and/or the carrier transport was significantly reduced during this period. This reduction could happen due to the formation of shallow traps and defects in the active layer as it aged in ambient air [96]. Considering the LUMO of water to be approximately -4 eV, it is similar to that of $PC_{61}BM$ and so water can potentially act as an extra acceptor material and capture electrons inside the active layer. However, without the necessary percolation path, these captured electrons cannot be transported and collected by the electrodes. As a result, the water molecules create shallow traps and reduce the carrier transport and photo current output in aged devices. Next, the decline in the forward bias current under dark condition was attributed to the oxidation of the Al electrode by the oxygen and water molecules coming in contact with the metallic electrode. This degradation of the electrodes could be easily observed as the surface of the Al electrode changed significantly with aging as shown in Fig. 5.3.

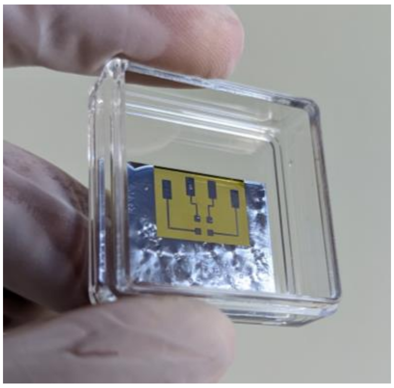

Fig. 5.3. Change in the Al electrode due to exposure to atmosphere.

5.2.2 Conventional Photodiode with Encapsulation

The previous results suggested that if the metallic electrodes and the organic layer can be well insulated from the atmospheric oxygen and water molecules, the performance of the photodetectors could be stabilized. This effect could be achieved by utilizing a barrier layer of polymer or resin to isolate the active layer from the surroundings.

With that objective in mind, the conventional photodiodes were encapsulated with a glass cover surrounded by epoxy glue (コニシボンド クイック５ エポキシ樹脂系接着剤) by the method described in Chapter 2.2.5. The devices were evaluated in the same fashion as above and the results are shown in the following figure.

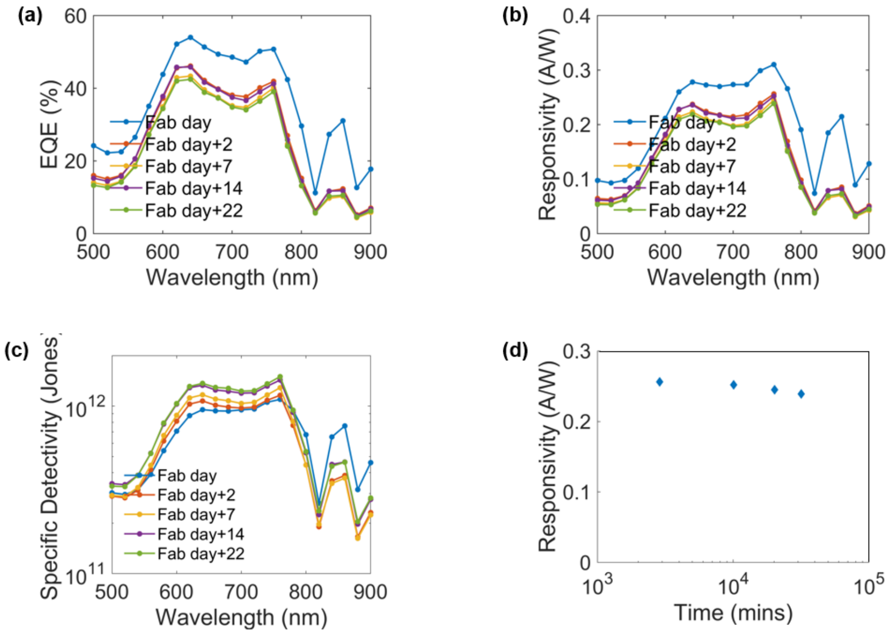

Fig. 5.4. (a) EQE, (b) R, (c) D^*_{sh} spectra and (d) change in R with respect to time of the encapsulated devices over a 23-day period.

As shown in Fig. 5.4 (a) and (b), the EQE and R values of the encapsulated devices stabilized approximately at 40% and 0.25 A/W respectively after the Fab day. The slight decline in EQE and R may have resulted from the air trapped inside encapsulated device and thus, from the second day onwards, these parameters did not show any significant degradation even after 22 days of fabrication. Compared to the Fab day to the 23rd day, the devices showed only 7% decrease in the value of R. On the other hand, D^*_{sh} value did not show any degradation at all, rather slightly improved in the encapsulated device suggesting that J_{dark} decreased but J_{photo} remained constant over this experimentation period. These results indicated that the glass cover and the epoxy glue worked as a good barrier layer against the atmospheric oxygen and water molecules and kept the active layer in pristine condition over a period of at least 23 days. For speculating the long-term stability of these devices, the gradual change in R was plotted with respect to the mins after fabrication as shown in Fig. 5.4 (d). The result is comparable to contemporary investigation on organic device stability and shows promise for accurate operation for more than 4 months [96]. It was concluded that by properly isolating the OPDs from atmosphere, the devices could be taken out of the controlled environment of research laboratory without risking the stability and reliability of their performance.

5.2.3 Inverted Photodiode

To counteract these effects of degradation the inverted photodiode structure was also thought to be a viable solution. In this case, the top electrode is Au which is a much more air stable metal compared to Al and thus, it might improve the air stability of the device by offering better protection from the atmosphere. To validate this assumption, inverted photodiodes were fabricated, and the devices was tested in a similar manner as described before for a period of 40 days after fabrication. The measurement data were collected over a span of 40 days, and they are shown as Fab day to Fab day+39 in Fig. 5.5.

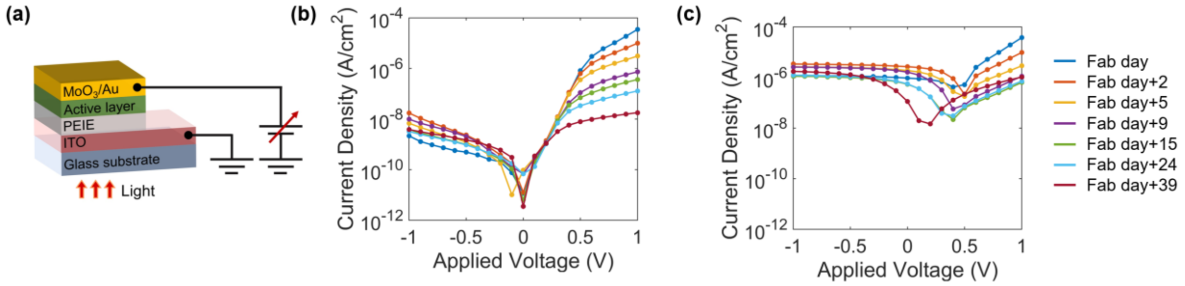

Figure 5.5. (a) Schematic illustration of the device, and current-voltage characteristics of the device under (b) dark and (c) illuminated condition over a 40-day period.

From the current-voltage characteristics, it could be clearly concluded that the inverted photodiodes showed much more stable performance compared to the conventional ones. Although the J_{dark} in reverse bias condition increased, and the J_{photo} in reverse bias decreased approximately 1 order of magnitude, it occurred within the span of 40 days. Even after the measurement period of 40 days, the photodetectors continued to operate which the conventional photodetectors without encapsulation were unable to do.

From these experiments, it was concluded that the performance of OPDs can be stabilized by keeping the metallic electrode and the organic layer away from atmospheric oxygen and water molecules. Fabricating OPDs in the inverted architecture was one of the viable solutions, but encapsulating the devices with a barrier layer was found as the best possible solution.

5.3 Necessary Figures of Merit

There are several figures of merit that are essential in order to make sure that the devices prepared inside the controlled environment of laboratories can indeed be used in practical applications. In this study, the final objective was to monitor the PPG signal of a human subject in ambient conditions, and in this case, practical photodetectors require fast transient response to ensure high rate of data collection. Fig. 5.6 (a) shows the transient photo response of the inverted OPDs as observed through the oscilloscope across a 10 kΩ resistor. The waveforms show that the OPDs were able to follow the input waveform up to 40 kHz, but the -3 dB point was found at approximately 3 kHz as shown in Fig. 5.6 (b). In this study, the capacitance of samples with an area of 1 mm^2 was approximately 44.3 pF. Considering the standard BNC cables with capacitance of 0.2 nF/m, the RC delay of the measurement system was less than 2 µsec. With this RC delay of the system, it could be concluded that the limiting factor of response speed was not the external capacitance of the system, rather the internal charge transport mechanism. A rough calculation showed that with this response speed, these PDs can capture 110 ppi video at a maximum of 30 fps. However, the objective biological signal of PPG has a range of 0.2 Hz to 2 Hz, thus the response speed of the OPDs was more than sufficient [97].

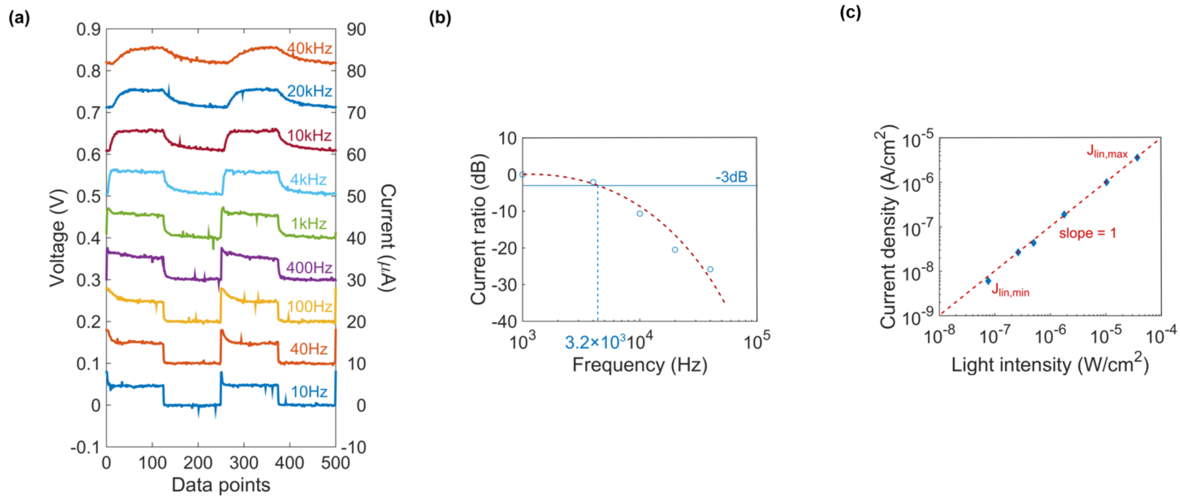

Figure 5.6. (a) Waveforms of the transient photo response, (b) cutoff frequency, and (c) LDR of the OPDs. The active area of the diode was 1 mm^2, and the diode was biased with -1 V.

In addition to sufficient response speed, the OPDs also showed very good LDR. As shown in Fig. 5.6 (c), the OPDs could detect the NIR irradiation from 80 nW/cm^2 to 36.9 µW/cm^2 and throughout the entire range, the output current followed a linear pattern with respect to the incident light intensity. Using a straight line of slope 1, the LDR was found to be at least 53.3 dB. This is a very typical value for organic OPDs, there are several reported OPDs with higher LDR [51, 15]. The limiting factor for this measurement is that the output of the xenon lamp cannot be increased beyond 36.9 µW/cm^2 for 740 nm. Therefore, the true LDR of these OPDs is expected to be much higher. As a result, the air stability, and figures of merit of cutoff frequency and LDR were within the necessary limit and the showed promise for the detection and monitoring of PPG spectrum.

5.4 Real Time Monitoring of PPG

After confirming the limit of the figures of merit and air stability of the devices, the practical usability of the OPD fabricated with the 1:1 sample was checked by measuring the PPG signal of a human subject in ambient conditions. The experimental setup for this measurement is schematically shown in Fig. 5.7 (a) where NIR light of 740 nm wavelength of 33 mW/cm^2 was emitted from an LED and the index finger of the volunteer was placed on top of the glass substrate of the OPD [98]. A fraction of the incident light was reflected at the blood vessels, another fraction was absorbed by the blood, and the remaining fraction was transmitted through the finger to the active layer of the OPD. As the arterial volume of the volunteer's blood changed with every heartbeat, the intensity of the reflected, absorbed, and transmitted NIR light also changed accordingly. Thus, if the NIR OPD positioned below the finger detected this intensity change of the transmitted light, the heartbeat of the volunteer could be observed, and the PPG signal could be monitored in real time.

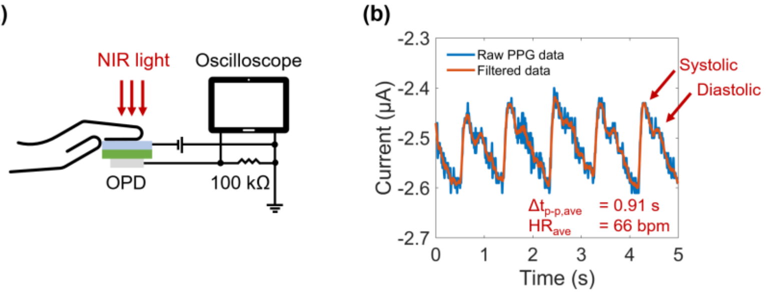

Fig. 5.7. (a) Schematic illustration of the monitoring system and (b) photoplethysmogram spectra of the subject before and after applying the moving average filter [98].

Figure 5.7 (b) shows the output of the OPD which demonstrates the successful monitoring of the PPG spectrum in real time. The unfiltered PPG spectrum contains environmental noise as the measurement setup was not completely isolated from electrical, optical, and acoustic interference. However, by applying a very simple moving average filter, the systolic and diastolic peaks of the heartbeat could be detected, and an average heartrate of 66 bpm could be extracted. This observation coincides with the contemporary measurement reports with organic and inorganic photodetectors [86, 99]. By utilizing a measurement system with better optical and electrical insulation from the surroundings, higher quality PPG signal can be obtained. In that case, the morphology of the PPG spectrum can be analyzed more effectively and valuable information about the subject's health and risk of cardiovascular diseases may be derived [100]. As this PPG measurement strategy uses NIR light, it has the potential to be used in both transmission and reflection mode making it a versatile option in biomedical applications.

5.5 Flexible and Wearable Device

One of the advantages of using organic semiconductors for device fabrication is the feasibility of preparing flexible devices. As flexible devices can be worn on body parts of human patients, it is both physically comfortable and technologically beneficial for gathering high resolution data. Thus, the devices in this study were also implemented on flexible PET substrates to be worn on the finger of human subjects. The target strain condition for the flexible devices were chosen to be at bending radius of 7.5 mm, which is similar to the radius of an average human index finger.

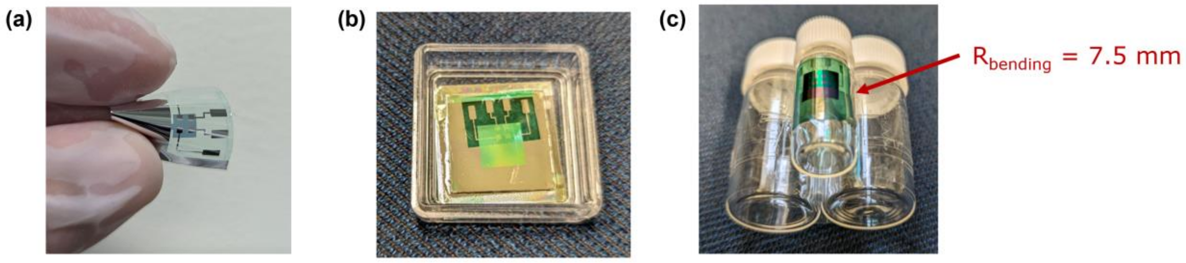

Fig. 5.8. (a) Flexible and wearable devices after fabrication, (b) fixed on a flat glass substrate and (c) fixed on a glass bottle with a bending radius of 7.5 mm.

The flexible devices were prepared with an inverted architecture with semitransparent Ag electrodes of 20 nm thickness. The Ag electrode showed nearly 50% transparency in the visible region as shown in Fig. 5.9. The transparency gradually decreased as the wavelength increased and was measured to be 27% at NIR wavelength of 740 nm.

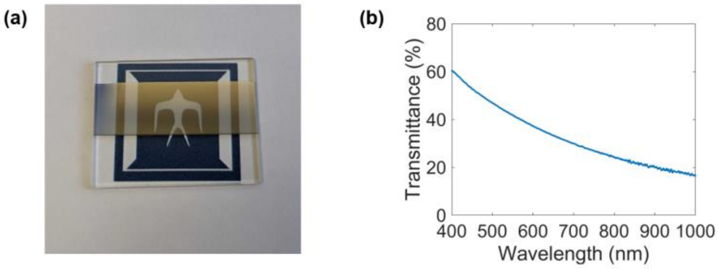

Fig. 5.9. (a) Semitransparent Ag electrode deposited on glass substrate and (b) transmittance spectra of the Ag electrode from visible to NIR wavelength.

In order to compare the performance of the flexible and wearable devices with rigid devices, photodetectors on top of glass substrates were prepared alongside the flexible devices. The current-voltage characteristics of all the devices are shown in the following figure.

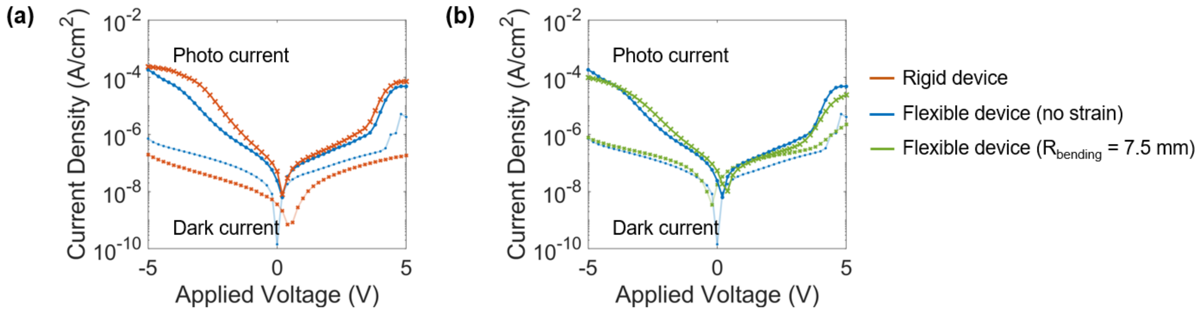

Fig. 5.10. Current-voltage characteristics (a) rigid and flexible devices with no strain, (b) flexible device with no strain and flexible device with a bending radius of 7.5 mm. The photo current was measured in ambient air with NIR light of 740 nm at 3.4 mW/cm^2.

As shown in Fig. 5.10, the dark current of the flexible device is approximately 1 order higher compared to that of the glass device. This may have originated because of the relatively rougher surface of the plastic substrate. If the surface of the substrate is rough, it may cause defects and pinholes in the solution processed active layer and cause an increase in the dark current. These defects might have also influenced the photo current output of the flexible device as it was lower in between the reverse bias voltage of 0 V to -5 V. The relatively low transparency of the 20 nm Ag electrode in the NIR region was also one of the reasons behind the low photo current output. In addition, the surface reflectance of the flexible device was also quite high as can be seen in the Fig. 5.8 (c). Due to this high surface reflectance, much of the incident light could not reach the active layer which resulted in the decreased photo current output. Due to these change in dark current and photo current, the rigid glass device showed better performance with EQE of 12% and D^*_{sh} of 2.8 × 10^{11} Jones at 740 nm at -5 V reverse bias. The values of these figures of merit for the flexible device were 9% and 1.1 × 10^{11} Jones, respectively. These measurements were carried out when the flexible was placed flat on a glass substrate without any strain. Measurements were also carried out when the flexible device was bent with a radius of 7.5 mm as shown in Fig. 5.8 (c). In this case, the device under strain did not show significant deviation from that of the flat device indicating very good mechanical flexibility of the devices. The overall comparison of all the devices is given in Table V.

Table V. Summary of figures of merit of photodetectors prepared on glass and flexible substrates. All the measurements are at 740 nm with -5 V reverse bias.

Sample name	J_{photo}/J_{dark}	R (mA/W)	EQE (%)	D^*_{sh} (Jones)
Rigid device	1.2×10^3	68.6	12%	2.8×10^{11}
Flexible device (No strain)	2.6×10^2	53.1	9%	1.1×10^{11}
Flexible device ($R_{bending}$ = 7.5 mm)	1.3×10^2	28.5	5%	5.7×10^{10}

5.6 Summary of Chapter 5

In this chapter, the performance of the champion OPD was analyzed on the basis of figures of merit and air stability to check if it is sufficient for the use in biomedical applications. The figures of cutoff frequency and linear dynamic range were found to be adequate, but the air stability of the conventional OPD was found to be very poor. This poor stability was attributed to the effect of atmospheric oxygen and water and two different strategies were proposed to increase the stability and reliability of the devices. By using inverted architecture with a counter electrode of stable metal i.e., Au, the stability was improved significantly and by encapsulating the device with epoxy glue and glass, even better results were obtained. The encapsulation method proved to be very effective as the OPD exhibited stable and reliable performance for more than a three-week period. After confirming the good performance and stability, the photoplethysmogram signal of a human subject was monitored in real time by using the champion device realized in this study. Although the monitoring system was relatively simple, the heartbeat rate of the subject could be extracted, and the systolic and diastolic peaks of the heartbeats were clearly detected after filtering the observed data with a moving average filter. The clarity of the observed spectrum underlined the practical utility of the NIR OPD of this study in biomedical applications. The realized PPG measurement strategy uses NIR light which can be used in both transmission and reflection mode of operation and makes this photodetector a versatile option in biomedical applications. As a final demonstration of mechanical flexibility of organic semiconductor-based devices, the OPD was implemented on plastic substrate of 25 µm thickness. The flexible devices showed 9% and 5% EQE under no strain and at bending radius of 7.5 mm, respectively.

Chapter 6

Conclusion and Outlook

6.1 Summary

In conclusion, solution processed near-infrared organic photodetectors with a liquid crystalline phthalocyanine derivative ($8H_2Pc$) with maximum external quantum efficiency of 60%, responsivity of 0.4 A/W, and shot-noise-limited specific detectivity of 3×10^{12} Jones at 760 nm were realized in this study. The performance of these bulk heterojunction organic photodetectors was superior to the ones prepared with soluble phthalocyanine derivative without any liquid crystalline phase ($8OH_2Pc$) suggesting the advantage of using liquid crystalline materials in photodetector applications. The better performance was attributed to the well intermixing of the donor and acceptor materials in the bulk heterojunction, creation of grains of tens of nm, and smooth surface morphology of the solution processed active layer. It was suggested that these advantageous bulk heterojunction conditions were achievable due to the weak intermolecular interaction and self-organizing nature of the liquid crystalline material. Careful interface engineering of diode electrodes proved to be very effective in lowering dark current levels and increasing reproducibility. One of the principal challenges of organic devices, poor air stability, was addressed and two different approaches to resolve the issue were demonstrated: inverted architecture photodiodes with a stable metal counter electrode and encapsulation of the device with epoxy glue and glass substrate. While the inverted photodiodes showed slower degradation of performance compared to conventional ones, epoxy glue and glass encapsulated photodiodes showed excellent stability and reliability with only 7% degradation in responsivity after 22 days of fabrication.

By thermal annealing at the liquid crystalline temperature of $8H_2Pc$, it was demonstrated that the molecules could be redirected from the edge-on orientation to the face-on orientation even after the deposition of the thin film. This reorientation of molecular direction significantly improved the device performance and photo current output of the photodetectors with neat $8H_2Pc$ active layer. The effect of thermal annealing at liquid crystalline and isotropic phases was also explored for the bulk heterojunction active layers and phase separation and change in grain size and purity of the donor and acceptor materials were observed. Annealing at isotropic temperature resulted in the face-on orientation of the disc-like molecules of $8H_2Pc$ but created large area grains in the order of tens of µm. On the other hand, annealing at liquid crystalline temperature achieved the effect of face-on orientation without creating such large grains. These changes could also be controlled by varying the duration of thermal annealing and the cooling rate of the samples from liquid crystalline phase to crystalline phase temperature. Furthermore, taking advantage of the solution process of active layer fabrication, flexible and wearable organic photodetectors were prepared on plastic substrates of 25 µm thickness. The flexible devices exhibited external quantum efficiency of 9% and 5% at 740 nm under no strain and at bending radius of 7.5 mm, respectively, indicating good mechanical flexibility and durability.

Finally, the practical utility of the near-infrared photodetectors was demonstrated by measuring the photoplethysmogram signal of a human subject in ambient conditions. By irradiating near-infrared light of 740 nm on the index finger of the subject, the systolic and diastolic peaks of the heartbeat could be detected in the filtered spectrum and an average heartrate of 66 bpm could be extracted. The accuracy of these results shows the prospect of these devices for utilization in hospitals and clinics in practical applications for the benefit of patients and elderly generation. As near-infrared light can penetrate deeper into biological tissue compared to visible light, the photodiodes could monitor the vital signals accurately in transmission mode of operation. This feature of using near-infrared light is advantageous because it can also be used in the reflection mode of operation which makes these photodetectors versatile in practical application. Furthermore, the flexible devices realized in this study may also be used in commercial products such as smartwatches or portable health monitors which will allow the users to have more freedom and comfort while monitoring their activities or vital signals.

6.2 General Conclusion

According to the results of this study, the following can be concluded:

- Bulk heterojunction condition differs significantly depending on the blend ratio of difference organic materials. By exploring the blend ratios, it is possible to vary the purity and size of the material grains, phase separation and intermixing condition, and surface morphology of the solution processed thin films.
- Liquid crystalline phthalocyanine derivative ($8H_2Pc$) based photodetectors showed better performance compared to the crystalline phthalocyanine derivative ($8OH_2Pc$) due to the well intermixing of the donor and acceptor materials in the bulk heterojunction, creation of grains of tens of nm, and smooth surface morphology of the

solution processed active layer. It was suggested that these advantageous bulk heterojunction conditions were achievable due to the soft and self-organized state of matter and weak intermolecular interaction of the liquid crystalline material.

- Thermal annealing at liquid crystalline temperature allows reorientation of columnar molecules from edge-on to face-on orientation even after deposition of the thin film. This effect can improve the performance of photodiodes due to the better charge carrier transport in the vertically aligned columnar direction. In a blend of liquid crystalline $8H_2Pc$ and amorphous $PC_{61}BM$, it was found that the melting point of the blend material is reduced compared to the neat materials. Depending on the temperature of thermal annealing, phase separation and change in grain size can be significantly different. While thermal annealing at isotropic phase temperature causes fast phase separation and creates large area grains, annealing at liquid crystalline temperature offers better control by causing relatively slower phase separation and smaller change in grain size.
- The reason behind failure of organic photodetectors is the exposure to atmospheric oxygen and water molecules which result in defects and shallow traps in the active layer and damage the top electrode due to oxidation. The shallow traps capture the photo generated carriers and reduce the current output of the photodetector. The work function of the damaged electrode changes and causes further degradation of performance. Inverted architecture of photodiodes and encapsulation of the device using a barrier layer to isolate the device from atmosphere are two effective ways to improve the air stability of organic photodetectors.

6.3 Future Outlook

In this study, near-infrared organic photodetectors based on a liquid crystalline phthalocyanine derivative were realized and their practical utility was demonstrated by monitoring the vital signal of a human subject. However, there are several issues that require further investigation for the clarification of underlying factors.

- According to the results of this study, performance of bulk heterojunction photodetectors improved significantly when the grain sizes approached tens of nm. However, the diffusion length of excitons could not be directly confirmed in the bulk heterojunction systems. It would be worthwhile to confirm the exciton diffusion length by the photoluminescence quenching method in the bulk heterojunction devices and correlate with the grain size.

- Although the flexible devices prepared in this study were operational, their performance was significantly poorer compared to the champion devices prepared on glass substrates. The underlying reasons were identified as high surface roughness of the plastic substrate, low transparency of the top electrode, and high surface reflectance of the device. By utilizing a planarization layer on top of the plastic substrate to reduce the surface roughness, using electrodes with better transparency, and polymer coating the device to reduce the reflectance, the performance of the flexible photodetectors may be improved in future experimentations.
- In this study, the solution processed thin films were deposited at room temperature and the effects of thermal annealing at liquid crystalline temperature were explored. However, the optimum duration and temperature of thermal annealing could not be determined with the amount of data gathered. As the thermal annealing process has been proven to improve the photodetector performance, optimization of the annealing process is a valuable research topic. Furthermore, deposition of the thin film at liquid crystalline temperature could not be explored within the framework of this study, which can also be investigated in the future.
- In this study, the objective value of EQE > 50% could be achieved with the LC $8H_2Pc$ based OPDs, however the values of $R > 0.5$ A/W and $D^*_{sh} > 10^{13}$ Jones could not be achieved with the current device configuration. By optimizing the thickness of the active layer and using more effective hole and electron blocking and transport layers, the performance of the devices may be improved further in future studies.

References

[1] A. Sandström, H. F. Dam, F. C. Krebs and L. Edman, "Ambient fabrication of flexible and large-area organic light-emitting devices using slot-die coating," *Nat Commun,* vol. 3, no. 1002, 2012.

[2] C. Lungenschmied, G. Dennler, H. Neugebauer, S. N. Sariciftci, M. Glatthaar, T. Meyer and A. Meyer, "Flexible, long-lived, large-area, organic solar cells," *Solar Energy Materials and Solar Cells,* vol. 91, no. 5, pp. 379-384, 2007.

[3] M. R. Niazi, R. Li, E. Q. Li, A. R. Kirmani, M. Abdelsamie, Q. Wang, W. Pan, M. M. Payne, J. E. Anthony, D.-M. Smilgies, S. T. Thoroddsen, E. P. Giannelis and A. Amassian, "Solution-printed organic semiconductor blends exhibiting transport properties on par with single crystals," *Nat Commun,* vol. 6, no. 8598, 2015.

[4] A. Pierre, I. Deckman, P. B. Lechêne and A. C. Arias, "High Detectivity All-Printed Organic Photodiodes," *Adv. Mater.,* vol. 27, pp. 6411-6417, 2015.

[5] S. Park, K. Fukuda, M. Wang, C. Lee, T. Yokota, H. Jin, H. Jinno, H. Kimura, P. Zalar, N. Matsuhisa, S. Umezu, G. C. Bazan and T. Someya, "Ultraflexible Near-Infrared Organic Photodetectors for Conformal Photoplethysmogram Sensors," *Adv. Mater.,* vol. 30, p. 1802359, 2018.

[6] M. S. White, M. Kaltenbrunner, E. D. Głowacki, K. Gutnichenko, G. Kettlgruber, I. Graz, S. Aazou, C. Ulbricht, D. A. M. Egbe, M. C. Miron, Z. Major, M. C. Scharber, T. Sekitani, T. Someya, S. Bauer and N. S. Sariciftci, "Ultrathin, highly flexible and stretchable PLEDs," *Nature Photonics,* vol. 7, pp. 811-816, 2013.

[7] R. Eckstein, T. Rödlmeier, T. Glaser, S. Valouch, R. Mauer, U. Lemmer and G. Hernandez-Sosa, "Aerosol-Jet Printed Flexible Organic Photodiodes: Semi-Transparent, Color Neutral, and Highly Efficient," *Adv. Electron. Mater.,* vol. 1, p. 1500101, 2015.

[8] B. Geffroy, P. l. Roy and C. Prat, "Organic light-emitting diode (OLED) technology: materials, devices and display technologies," *Polym Int,* vol. 55, pp. 572-582, 2006.

[9] S. O. Jeon, K. H. Lee, J. S. Kim, S.-G. Ihn, Y. S. Chung, J. W. Kim, H. Lee, S. Kim, H. Choi and J. Y. Lee, "High-efficiency, long-lifetime deep-blue organic light-emitting diodes," *Nat. Photonics*, vol. 15, p. 208–215, 2021.

[10] M. Riede, D. Spoltore and K. Leo, "Organic Solar Cells—The Path to Commercial Success," *Adv. Energy Mater.,* vol. 2002653, p. 11, 2021.

[11] X. Liu, Y. Lin, Y. Liao, J. Wu and Y. Zheng, "Recent advances in organic near-infrared photodiodes," *J. Mater. Chem. C,* vol. 6, p. 3499, 2018.

[12] C. W. Tang, "Two-layer organic photovoltaic cell," *Appl. Phys. Lett.,* vol. 48, pp. 183-185, 1986.

[13] M. A. Green, A. Ho-Baillie and H. J. Snaith, "The emergence of perovskite solar cells," *Nat. Photon.,* vol. 8, p. 506–514, 2014.

[14] Y. Rong, Y. Hu, A. Mei, H. Tan, M. I. Saidaminov, S. I. Seok, M. D. McGehee, E. H. Sargent and H. Han, "Challenges for commercializing perovskite solar cells," *Science,* vol. 361, p. 1214, 2018.

[15] Z. Zhong, K. Li, J. Zhang, L. Ying, R. Xie, G. Yu, F. Huang and Y. Cao, "High-Performance All-Polymer Photodetectors via a Thick Photoactive Layer Strategy," *ACS Appl. Mater. Interfaces,* vol. 11, p. 14208−14214, 2019.

[16] G. Yu, J. Gao, J. C. Hummelen, F. Wudl and A. J. Heeger, "Polymer Photovoltaic Cells: Enhanced Efficiencies via a Network of Internal Donor-Acceptor Heterojunctions," *Science,* vol. 270, pp. 1789-1791, 1995.

[17] J. J. M. Halls, C. A. Walsh, N. C. Greenham, E. A. Marseglia, R. H. Friend, S. C. Moratti and A. B. Holmes, "Efficient photodiodes from interpenetrating polymer networks," *Nature,* vol. 376, pp. 498-500, 1995.

[18] Z. Zhao, M. Liu, K. Yang, C. Xu, Y. Guan, X. Ma, J. Wang and F. Zhang, "Highly Sensitive Narrowband Photomultiplication-Type Organic Photodetectors Prepared by Transfer-Printed Technology," *Adv. Funct. Mater.,* vol. 31, p. 2106009, 2021.

[19] A. Armin, R. D. J.-v. Vuuren, N. Kopidakis, P. L. Burn and P. Meredith, "Narrowband light detection via internal quantum efficiency manipulation of organic photodiodes," *Nat Commun,* vol. 6, no. 6343, 2015.

[20] M. Liu, J. Wang, Z. Zhao, K. Yang, P. Durand, F. Ceugniet, G. Ulrich, L. Niu, Y. Ma, N. Leclerc, X. Ma, L. Shen and F. Zhang, "Ultra-Narrow-Band NIR Photomultiplication Organic Photodetectors Based on Charge Injection Narrowing," *J. Phys. Chem. Lett.,* vol. 12, no. 11, p. 2937–2943, 2021.

[21] Z. Wu, W. Yao, A. E. London, J. D. Azoulay and T. N. Ng, "Elucidating the Detectivity Limits in Shortwave Infrared Organic Photodiodes," *Adv. Funct. Mater.,* vol. 28, p. 1800391, 2018.

[22] H. Ren, J.-D. Chen, Y.-Q. Li and J.-X. Tang, "Recent Progress in Organic Photodetectors and their Applications," *Adv. Sci.,* vol. 8, p. 2002418, 2021.

[23] M. Liu, K. Yang, Z. Zhao, Z. Zhou, X. Ma, J. Wang and F. Zhang, "Narrowband Photomultiplication Organic Photodetectors by Employing Phosphorescent Material as Optical Field Adjusting Layer," *J. Phys. Chem. C,* vol. 125, p. 18536−18542, 2021.

[24] Z. Zhao, C. Li, L. Shen, X. Zhang and F. Zhang, "Photomultiplication type organic photodetectors based on electron tunneling injection," *Nanoscale,* vol. 12, p. 1091, 2020.

[25] H. Xu, J. Liu, J. Zhang, G. Zhou, N. Luo and N. Zhao, "Flexible Organic/Inorganic Hybrid Near-Infrared Photoplethysmogram Sensor for Cardiovascular Monitoring," *Adv. Mater.,* vol. 29, p. 1700975, 2017.

[26] T. Yokota and et.al., "Ultraflexible, large-area, physiological temperature sensors for multipoint measurements," *PNAS,* vol. 112, no. 47, p. 14533–14538, 2015.

[27] M. Ohmori, Y. Nishikawa, A. Fujii and M. Ozaki, "Homeotropic alignment of non-peripheral octahexyl phthalocyanine in thin film and its photovoltaic properties," *Jpn. J. Appl. Phys.,* vol. 57, p. 08RE02 , 2018.

[28] M. Ohmori, H. Fukui, Q.-D. Dao, T. Kumada, A. Fujii, Y. Shimizu and M. Ozaki, "Annealing effect in bulk heterojunction organic solar cells utilizing liquid crystalline phthalocyanine," *Jpn. J. Appl. Phys.,* vol. 53, p. 05FZ02, 2014.

[29] H. Iino, T. Usui and J.-i. Hanna, "Liquid crystals for organic thin-film transistors," *Nature Communications,* vol. 6, p. 6828, 2015.

[30] S. Sergeyev, W. Pisula and Y. H. Geerts, "Discotic liquid crystals: a new generation of organic semiconductors," *Chem. Soc. Rev.,* vol. 36, pp. 1902-1929, 2007.

[31] E. Pouzet and et.al., "Homeotropic Alignment of a Discotic Liquid Crystal Induced by a Sacrificial Layer," *J. Phys. Chem. C,* vol. 113, p. 14398–14406, 2009.

[32] H. Iino and J.-i. Hanna, "Availability of Liquid Crystallinity in Solution Processing for Polycrystalline Thin Films," *Adv. Mater.,* vol. 23, p. 1748–1751, 2011.

[33] M. Roser, H. Ritchie, E. Ortiz-Ospina and L. Rodés-Guirao, "World Population Growth," 2013. [Online]. Available: https://ourworldindata.org/world-population-growth. [Accessed 16 12 2022].

[34] D. B. Wayne, M. Green and E. G. Neilson, "Medical education in the time of COVID-19," *Science Advances,* vol. 6, no. 31, p. eabc7110, 2020.

[35] P. Chibber, S. A. Haq, I. Ahmed, N. I. Andrabi and G. Singh, "Advances in the possible treatment of COVID-19: A review.," *European Journal of Pharmacology,* vol. 883, p. 173372, 2020.

[36] P. Peumans, A. Yakimov and S. R. Forrest, "Small molecular weight organic thin-film photodetectors and solar cells," *J. Appl. Phys.,* vol. 93, p. 3693, 2003.

[37] Y. Zhou and et.al., "A Universal Method to Produce Low–Work Function Electrodes for Organic Electronics," *Science,* vol. 336, no. 6079, pp. 327-332, 2012.

[38] X. Deng and et.al., "Ultra-Low Work Function Transparent Electrodes Achieved by Naturally Occurring Biomaterials for Organic Optoelectronic Devices," *Adv. Mater. Interfaces,* vol. 1, p. 1400215, 2014.

[39] A. Armin, M. Velusamy, P. Wolfer, Y. Zhang, P. L. Burn, P. Meredith and A. Pivrikas, "Quantum Efficiency of Organic Solar Cells: Electro-Optical Cavity Considerations," *ACS Photonics*, vol. 1, no. 3, p. 173–181, 2014.

[40] G. Juška, N. Nekrašas and K. Genevičius, "Investigation of charge carriers transport from extraction current transients of injected charge carriers," *Journal of Non-Crystalline Solids*, vol. 358, pp. 748-750, 2012.

[41] P. Jonsson, J. Casselgren and B. Thörnberg, "Road Surface Status Classification Using Spectral Analysis of NIR Camera Images," *IEEE SENSORS JOURNAL*, vol. 15, p. 1641, 2015.

[42] D. Hertel, H. Marechal, D. A. Tefera, W. Fan and R. Hicks, "A low-cost VIS-NIR true color night vision video system based on a wide dynamic range CMOS imager," *IEEE Intelligent Vehicles Symposium*, pp. 273-278, 2009.

[43] M. S. Millán and J. Escofet, "Fabric inspection by near-infrared machine vision," *Opt. Lett.*, vol. 29, pp. 1440-1442, 2004.

[44] X. Fu and Y. Ying, "Food Safety Evaluation Based on Near Infrared Spectroscopy and Imaging: A Review," *Critical Reviews in Food Science and Nutrition*, vol. 56, no. 11, pp. 1913-1924, 2016.

[45] R. Weissleder, "A clearer vision for in vivo imaging," *Nat Biotechnol*, vol. 19, pp. 316-317, 2001.

[46] P. K. Upputuri and M. Pramanik, "Photoacoustic imaging in the second near-infrared window: a review," *Journal of Biomedical Optics*, vol. 24, no. 4, p. 040901, 2019.

[47] Z. Wu, W. Yao, A. E. London, J. D. Azoulay and T. N. Ng, "Elucidating the Detectivity Limits in Shortwave Infrared Organic Photodiodes," *Adv. Funct. Mater.*, vol. 28, p. 1800391, 2018.

[48] H. W. Yoon, M. C. Dopkiss and G. P. Eppeldauer, "Performance comparisons of InGaAs, extended InGaAs, and short-wave HgCdTe detectors between 1 μm and 2.5 μm," *Proc. SPIE 6297, Infrared Spaceborne Remote Sensing XIV*, p. 629703, 2006.

[49] Q. Lin, A. Armin, P. L. Burn and P. Meredith, "Near infrared photodetectors based on sub-gap absorption in organohalide perovskite single crystals," *Laser Photonics Rev.*, vol. 10, p. 1047, 2016.

[50] M. J. Cook, A. J. Dunn, S. D. Howe and A. J. Thomson, "Octa-al koxy Phthalocyanine and Naphthalocyan ine Derivatives: Dyes with Q-Band Absorption in the Far Red or Near Infrared," *J. Chem. Soc. Trans. 1,* 1988.

[51] J. Huang, J. Lee, J. Vollbrecht, V. V. Brus, A. L. Dixon, D. X. Cao, Z. Zhu, Z. Du, H. Wang, K. Cho, G. C. Bazan and T.-Q. Nguyen, "A High-Performance Solution-Processed Organic Photodetector for Near-Infrared Sensing," *Adv.Mater.,* vol. 32, p. 1906027, 2020.

[52] R. Fujioka, T. Fukushima, N. Oishi, Y. Koshiba, C. Takechi, S. Horike, H. Kaji and K. Ishida, "Improving NIR sensor detectivity of BODIPY/C60 bulk heterojunction photodiode," *Jpn. J. Appl. Phys.,* vol. 59, p. SGGG04, 2019.

[53] C. Fuentes-Hernandez, W.-F. Chou, T. M. Khan, L. Diniz, J. Lukens, F. A. Larrain, V. A. Rodriguez-Toro and B. Kippelen, "Large-area low-noise flexible organic photodiodes for detecting faint visible light," *Science*, vol. 370, p. 698–701, 20202.

[54] X. Ren, K. Pei, B. Peng, Z. Zhang, Z. Wang, X. Wang and P. K. L. Chan, "A Low-Operating-Power and Flexible Active-Matrix Organic-Transistor Temperature-Sensor Array," *Adv. Mater.*, vol. 28, p. 4832–4838, 2016.

[55] T. N. Ng, W. S. Wong, M. L. Chabinyc, S. Sambandan and R. A. Street, "Flexible image sensor array with bulk heterojunction organic photodiode," *Appl. Phys. Lett.,* vol. 92, p. 213303, 2008.

[56] "Si PIN photodiodes," S.S.D. Hamamatsu Photonics K.K, [Online]. Available: https://www.hamamatsu.com/content/dam/hamamatsu-photonics/sites/documents/99_SALES_LIBRARY/ssd/s8385_etc_kpin1064e.pdf. [Accessed 20 December 2022].

[57] A. Köhler and H. Bässler, Electronic Processes in Organic Semiconductors, Wiley-VCH, 2015.

[58] B. Lüssem, C.-M. Keum, D. Kasemann, B. Naab, Z. Bao and K. Leo, "Doped Organic Transistors," *Chem. Rev.*, vol. 116, no. 22, p. 13714–13751, 2016.

[59] B. Kang, W. H. Lee and K. Cho, "Recent Advances in Organic Transistor Printing Processes," *ACS Appl. Mater. Interfaces*, vol. 5, no. 7, p. 2302–2315, 2013.

[60] T. M. Clarke and J. R. Durrant, "Charge Photogeneration in Organic Solar Cells," *Chem. Rev. 2010*, vol. 110, no. 11, p. 6736–6767, 2010.

[61] F. Arca, "Organic photodiodes for industrial sensing and medical imaging, PhD Dissertation," The Technical University of Munich, 2013, Munich, 2013.

[62] M. Jaiswal and R. Menon, "Polymer electronic materials: a review of charge transport," *Polymer International*, vol. 55, no. 12, pp. 1371-1384, 2006.

[63] A. S. Cherodian, A. N. Davies, R. M. Richardson, M. J. Cook, N. B. McKeown, A. J. Thomson, J. Feijoo, G. Ungar and J. Harrison, "Mesogenic Behaviour of some 1,4,8,11,15,18,22,25-Octa-alkylphthalocyanines," *Molecular Crystals and Liquid Crystals*, vol. 196, no. 1, pp. 103-114, 1991.

[64] H. Iino, J.-i. Hanna, R. J. Bushby, B. Movaghar, B. J. Whitaker and M. J. Cook, "Very high time-of-flight mobility in the columnar phases of a discotic liquid crystal," *Appl. Phys. Lett.*, vol. 87, p. 132102, 2005.

[65] R. Barberi and G. Durand, "Order parameter of a nematic liquid crystal on a rough surface," *Physical Review A*, vol. 41, no. 4, 1990.

[66] J. K. Vij, A. Kocot and T. S. Perova, "Order Parameter, Alignment and Anchoring Transition in Discotic Liquid Crystals," *Mol. Cryst. Liq. Cryst.*, vol. 397, p. 231/[531]–244/[544], 2003.

[67] A. R. Zanatta, "Revisiting the optical bandgap of semiconductors and the proposal of a unified methodology to its determination," *Scientific Reports*, vol. 9, p. 11225, 2019.

[68] J. I. Pankove, Optical processes in semiconductors, New York: Dover Pub., 1971.

[69] S. Kabir, Y. Takayashiki, J.-i. Hanna and H. Iino, "Solution processed near-infrared organic photodetector based on a liquid crystalline phthalocyanine derivative for vital signal monitoring," *Jpn. J. Appl. Phys.,* 2022.

[70] S. Kabir, Y. Takayashiki, A. Ohno, J.-i. Hanna and H. Iino, "Near-infrared organic photodetectors with a soluble Alkoxy-Phthalocyanine derivative," *Optical Materials,* vol. 126, p. 112209, 2022.

[71] M. Hiramoto, K. Kitada, K. Iketaki and T. Kaji, "Near infrared light driven organic p-i-n solar cells incorporating phthalocyanine J-aggregate," *Appl. Phys. Lett.,* vol. 98, p. 023302 , 2011.

[72] M. Ozaki, M. Yoneya, Y. Shimizu and A. Fujii, "Carrier transport and device applications of the organic semiconductor based on liquid crystalline non-peripheral octaalkyl phthalocyanine," *Liquid Crystals,* vol. 45, no. 13-15, pp. 2376-2389, 2018.

[73] T. K. Mullenbach, I. J. Curtin, T. Zhang and R. J. Holmes, "Probing dark exciton diffusion using photovoltage," *Nat Commun,* vol. 8, p. 14215, 2017.

[74] D. Chirvase, J. Parisi, J. C. Hummelen and V. Dyakonov, "Influence of nanomorphology on the photovoltaic action of polymer–fullerene composites," *Nanotechnology* , vol. 15 , p. 1317–1323, 2004.

[75] T. Hori, Y. Miyake, N. Yamasaki, H. Yoshida, A. Fujii, Y. Shimizu and M. Ozaki, "Solution Processable Organic Solar Cell Based on Bulk Heterojunction Utilizing Phthalocyanine Derivative," *Appl. Phys. Express,* vol. 3, p. 101602, 2010.

[76] K. Fukumura, T. Hori, T. Masuda, D. Q. Duy, A. Fujii, Y. Shimizu and M. Ozaki, "Solvent Effects on Solution-Processable Bulk Heterojunction Organic Solar Cells Utilizing 1,4,8,11,15,18,22,25-Octahexylphthalocyanine," *Jpn. J. Appl. Phys.,* vol. 52, p. 05DB02, 2013.

[77] Y. Fang, A. Armin, P. Meredith and J. Huang, "Accurate characterization of next-generation thin-flm photodetectors," *Nature Photonics,* vol. 13, pp. 1-4, 2019.

[78] O. V. Mikhnenko, P. W. M. Blom and T.-Q. Nguyen, "Exciton diffusion in organic semiconductors," *Energy Environ. Sci.,* vol. 8, pp. 1867-1888, 2015.

[79] X.-Y. Zhu, Q. Yang and M. Muntwiler, "Charge-Transfer Excitons at Organic Semiconductor Surfaces and Interfaces," *Acc. Chem. Res.,* vol. 42, no. 11, p. 1779–1787, 2009.

[80] Z. Zhao, B. Liu, C. Xu, M. Liu, K. Yang, X. Zhang, Y. Xu, J. Zhang, W. Li and F. Zhang, "Highly sensitive all-polymer photodetectors with ultraviolet-visible to near-infrared photodetection and their application as an optical," *J. Mater. Chem. C,* vol. 9, p. 5349, 2021.

[81] K. Yang, Z. Zhao, M. Liu, Z. Zhou, K. Wang, X. Ma, J. Wang, Z. He and F. Zhang, "Employing liquid crystal material as regulator to enhance performance of photomultiplication type polymer photodetectors," *Chemical Engineering Journal,* vol. 427, p. 131802, 2022.

[82] G. Simone, M. J. Dyson, S. C. J. Meskers, R. A. J. Janssen and G. H. Gelinck, "Organic Photodetectors and their Application in Large Area and Flexible Image Sensors: The Role of Dark Current," *Adv. Funct. Mater.,* p. 1904205, 2019.

[83] X. Gong, M.-H. Tong, S. H. Park, M. Liu, A. Jen and A. J. Heeger, "Semiconducting Polymer Photodetectors with Electron and Hole Blocking Layers: High Detectivity in the Near-Infrared," *Sensors,* vol. 10, pp. 6488-6496, 2010.

[84] B. A. E. Courtright and S. A. Jenekhe, "Polyethylenimine Interfacial Layers in Inverted Organic Photovoltaic Devices: Effects of Ethoxylation and Molecular Weight on Efficiency and Temporal Stability," *ACS Appl. Mater. Interfaces,* vol. 7, p. 26167−26175, 2015.

[85] 安達千波矢, 有機半導体のデバイス物性, 東京: 講談社, 2012.

[86] A. Joseph, A. B. Pillai, V. K. Pulikodan, A. Alexander, R. Muhammed and M. A. G. Namboothiry, "Solution-Processed Self-Powered Panchromatic Organic Photodiode and Its Application in Biomedical Devices," *ACS Appl. Electron. Mater.,* vol. 4, no. 4, p. 1567–1575, 2022.

[87] H. Kim, B. Song, K. Lee, S. Forrest and J. Kanicki, "Bilayer Interdiffused Heterojunction Organic Photodiodes Fabricated by Double Transfer Stamping," *Adv. Optical Mater.,* p. 1600784, 2017.

[88] E. Grelet and H. Bock, "Control of the orientation of thin open supported columnar liquid crystal films by the kinetics of growth," *Europhys. Lett.,* vol. 73, no. 5, p. 712–718, 2006.

[89] D. Castaneda, A. Esparza, M. Ghamari, C. Soltanpur and H. Nazeran, "A review on wearable photoplethysmography sensors and their potential future applications in health care," *Int J Biosens Bioelectron.,* vol. 4, no. 4, pp. 195-202, 2018.

[90] T. Tamura, Y. Maeda, M. Sekine and M. Yoshida, "Wearable Photoplethysmographic Sensors—Past and Present," *Electronics,* vol. 3, no. 2, pp. 282-302, 2014.

[91] J. Přibil, A. Přibilová and I. Frollo, "Comparative Measurement of the PPG Signal on Different Human Body Positions by Sensors Working in Reflection and Transmission Modes," *Eng. Proc.,* vol. 2, no. 69, 2020.

[92] S. Wu and H.-J. Butt, "Near-infrared photochemistry at interfaces based on upconverting nanoparticles," *Phys. Chem. Chem. Phys.,* vol. 19, pp. 23585-23596, 2017.

[93] A. V. Moço, S. Stuijk and G. d. Haan, "New insights into the origin of remote PPG signals in visible light and infrared," *Sci Rep,* vol. 8, no. 8501, 2018.

[94] N. Sviridova and K. Sakai, "Human photoplethysmogram: new insight into chaotic characteristics," *Chaos, Solitons & Fractals,* vol. 77, pp. 53-63, 2015.

[95] M. Falter, W. Budts, K. Goetschalckx, V. Cornelissen and R. Buys, "Accuracy of Apple Watch Measurements for Heart Rate and Energy Expenditure in Patients With Cardiovascular Disease: Cross-Sectional Study," *JMIR Mhealth Uhealth,* vol. 7, no. 3, p. e11889, 2019.

[96] M. Kielar, M. Daanoune, O. François-Martin, B. Flament, O. Dhez, A. K. Pandey, S. Chambon, R. Clerc and L. Hirsch, "Insights into the Failure Mechanisms of Organic Photodetectors," *Adv. Electron. Mater.,* vol. 4, no. 2, p. 1700526, 2018.

[97] R. A. Cernat, C. Ungureanu, G. M. Ungureanu, R. Aarts and J. Arends, "Real-time extraction of the respiratory rate from photoplethysmographic signal using wearable devices," in *European Conference on Ambient Intelligence*, Eindhoven, 2014.

[98] S. Kabir, Y. Takayashiki, J.-i. Hanna and H. Iino, "Near-infrared Photodetectors Based on a Liquid Crystalline Organic Semiconductor for Photoplethysmography Applications," in *2022 IEEE Sensors*, Dallas, TX, 2022.

[99] G. Simone, D. Tordera, E. Delvitto, B. Peeters, A. J. J. M. v. Breemen, S. C. J. Meskers, R. A. J. Janssen and G. H. Gelinck, "High-Accuracy Photoplethysmography Array Using Near-Infrared Organic Photodiodes with Ultralow Dark Current," *Adv. Optical Mater.*, vol. 8, p. 1901989, 2020.

[100] H. Akkerman, B. Peeters, A. v. Breemen, S. Shanmugam, L. U. Lopez, D. Tordera, E. Delvitto, G. Simone, R. v. d. Ketterij, A. J. Kronemeijer, E. Meulenkamp and G. Gelinck, "Measuring Health Parameters with Large-Area Organic Photodetector Arrays," *Society of Information Display International Symposium*, vol. 52, no. 1, pp. 41-44, 2021.

Publications

Journal Papers

- "Near-infrared organic photodetectors with a soluble Alkoxy-Phthalocyanine derivative", S. Kabir, Y. Takayashiki, A. Ohno, J. Hanna & H. Iino, Optical Materials, Vol. 126, April 2022, 112209.
- "Solution-processed near-infrared organic photodetector based on a liquid crystalline phthalocyanine derivative for vital signal monitoring", S. Kabir, Y. Takayashiki, J. Hanna & H. Iino, Jpn. J. Appl. Phys. 62 SC1013 (2023).

Conference Presentations

- S. Kabir, Y. Takayashiki, J. Hanna, H. Iino, "Near-infrared Photodetectors Based on a Liquid Crystalline Organic Semiconductor for Photoplethysmography Applications", Poster presentation, The 2022 IEEE Sensors Conference, Dallas, TX, USA.
- S. Kabir, Y. Takayashiki, J. Hanna, H. Iino, "Study of Near-infrared Organic Photodetectors with Octa-substituted Alkyl and Alkoxy Phthalocyanine Derivatives", Oral presentation, The 2022 International Conference on Solid State Devices and Materials (SSDM2022), Chiba, Japan.
- S. Kabir, Y. Takayashiki, J. Hanna, H. Iino, "Study on wearable near-infrared photodetectors based on a liquid crystalline organic semiconductor material for medical imaging", Oral presentation, The 69th JSAP Spring Meeting 2022, online.
- S. Kabir, Y. Takayashiki, M. Yang, J. Hanna, and H. Iino, "Near-infrared Light Detection with Organic Photodetectors based on Phthalocyanine Derivatives", Oral presentation, 2021 IEICE General Conference, online.
- S. Kabir, Y. Takayashiki, J. Hanna, and H. Iino, "Solution-processed Near-infrared Photodetector Based on a Liquid Crystalline Organic Semiconductor Material", Oral presentation, The 2020 International Conference on Solid State Devices and Materials (SSDM2020), online.
- S. Kabir, Y. Takayashiki, J. Hanna, and H. Iino, "Performance Study of Near-Infrared Organic Photodetectors based on a Phthalocyanine Derivative and a Fullerene

Derivative with Different Blend Ratios", Poster presentation, The 80th JSAP Autumn Meeting 2019, Hokkaido, Japan.

- S. Kabir, Y. Takayashiki, J. Hanna, and H. Iino, "Improvement of Near Infra-Red Imaging Sensor Performance by Using the Liquid Crystalline Properties of a Phthalocyanine Derivative", Poster presentation, International Conference on Advanced Imaging, Chiba, Japan.
- S. Kabir, Y. Takayashiki, J. Hanna, and H. Iino, "Near Infra-Red Organic Photodetectors Based on a Liquid Crystalline Phthalocyanine Derivative for Medical Imaging Purpose", Oral presentation, The 10th International Conference on Molecular Electronics and Bioelectronics 2019, Nara, Japan.

Acknowledgement

This thesis is based on the research work carried out during the Master and Doctor course at Imaging Science and Engineering Laboratory, Tokyo Institute of Technology, Japan, from April 2018 to March 2023, under the supervision of Professor Hiroaki Iino.

First of all, I would like to thank my supervisor, Professor Hiroaki Iino, for his continuous guidance, fruitful discussions, spending many hours proofreading my thesis and other publications, always giving me valuable advice and suggestions, and warm encouragement throughout this study. I sincerely appreciate his kind understanding and thoughtful supervision during and after the very the difficult situation because of the COVID-19 pandemic.

I would also like to thank Professor Jun-ichi Hanna and Professor Akira Ohno for their valued comments and suggestions, and helpful discussions during the research meetings every month for five years. Their experienced suggestions and critical discussions provided me many new ideas and I learned how to explore different areas to find answers instead of getting stuck in a singular way of thinking and performing research.

I would like to thank Ms. Yukiko Takayashiki for the synthesis and purification of various organic materials necessary for this study and helpful discussions related to the physical and chemical nature of such materials and material systems.

I would like to thank Dr. Masashi Miyakawa of NHK Science & Technology Research Laboratories for guidance and discussion on the measurement of photodetector parameters at the research laboratory.

I would like to thank Professor Kotaro Kajikawa, Professor Takaaki Manaka, and Professor Shinsuke Miyajima for valuable comments throughout my Master and Doctor studies and judgement of my thesis.

I am grateful to Ms. Rumi Tokuoka for her wholehearted generosity and genuine kindness and taking care of various administrative procedures and documents during the last five years.

I would also like to thank the members of Iino Laboratory, my seniors for their guidance and advice, and my colleagues and juniors for their comments and suggestions on my research theme and assistance on the vital signal monitoring of a human subject.

I was also very lucky to have a few truly good friends outside of the laboratory. I had the chance to discuss honestly and deeply with them during my time at this university and could learn so much from their diverse and unique experiences and opinions. I am grateful to each and every one of them for their friendship.

I would also like to thank Professor Yuri Matsuzaki and Professor Kenshu Kamura of Tokyo Tech Academy for Leadership (ToTAL) for their earnest mentorship and guidance. During my four-year affiliation with ToTAL, I received numerous opportunities to learn and practice facilitation, teamwork, and leadership and I consider these lessons as important as my graduate studies. I am thankful to all the professors and staff members of ToTAL for creating such a wonderful learning opportunity.

Finally, I would like to express my heartfelt gratitude to my family members in my home country, Bangladesh, and Ohka family here in Japan for their never-ending support and encouragement throughout my graduate studies.

Shahriar Kabir

Dedicated to my family